Applied Thermal Engineering 268 (2025) 125848

Contents lists available at ScienceDirect

Applied Thermal Engineering

journal homepage: www.elsevier.com/locate/apthermeng

Research Paper

Innovative hybrid battery thermal management system incorporating copper foam porous fins and layers with phase change material and liquid cooling

Alireza Keyhani-Asl, Noel Perera [*], Jens Lahr, Reaz Hasan

College of Engineering, Faculty of Computing, Engineering and the Built Environment, Birmingham City University, Birmingham B4 7XG, UK

ARTICLE INFO

Keywords:
Hybrid battery thermal management system
Phase change material
Copper foam
Liquid cooling
Energy density
Lithium-ion battery

ABSTRACT

In the present numerical investigation, a hybrid battery thermal management system (HBTMS) has been studied which combines phase change material (PCM), copper foam as porous fins and porous layers, and liquid cooling. The system includes twelve 18,650 Lithium-ion batteries encased in aluminium housing, with copper foam used as longitudinal porous fins within the PCM and as porous layer inside copper tubes within the cooling plates. The enthalpy-porosity model was employed for PCM simulation, and the Darcy-Brinkman-Forchheimer (DBF) model was used for copper foam. Local thermal equilibrium (LTE) and non-equilibrium (LTNE) models were utilized to simulate the porous fins and layers, respectively. Transient heat generation was considered based on a lumped-capacitance thermal model. This study addresses a key research gap by optimising the properties of porous fins and layers to enhance both passive and active cooling mechanisms, to effectively improve both thermal performance and energy density. The obtained results indicated the superior performance of porous fins compared to solid fins. The proposed HBTMS significantly reduces the maximum battery surface temperature by up to 9.18 K at a 5C discharge rate compared to pure PCM battery thermal management system (BTMS), while maintaining maximum temperature difference within the battery pack below 1 K, even at high 5C discharge rate. While porous fins with lower porosity improves conduction in the PCM, porous layers with higher porosity enhances convection within the copper tubes. Also, the utilization of porous fins, compared to solid fins, improves the energy density of the system by approximately 25 %.

1. Introduction

The growing concerns regarding carbon emissions resulting from the utilization of fossil fuels has compelled the implementation of environmental measures, particularly in the transportation sector, which plays a substantial role in the carbon footprint. Electric vehicles (EVs) and hybrid electric vehicles (HEVs) have become feasible options in this situation for tackling pollution and emissions by utilizing battery power. Nevertheless, the extensive implementation of EVs presents challenges, particularly in the areas of battery efficiency and thermal control. The performance of lithium-ion batteries (LIBs) as an appropriate option for EVs and HEVs, is significantly influenced by temperature. Low temperatures have a negative impact on the performance of batteries, leading to a decrease in their charge acceptance, store energy and power, and overall lifespan [1–3]. Elevated temperatures, conversely, diminish capacity, shorten lifespan, and cause safety hazards such as thermal runaway [4–6]. LIBs operate best at temperatures between 15 °C and 35 °C [7], or 20 °C and 40 °C [8,9], or 20 °C and 50 °C [10,11]. The maximum temperature difference (ΔT_{max}) among modules should also be smaller than 5 °C in order to provide a consistent temperature distribution [9,12–14]. Under typical operating circumstances, 60 °C has been reported to be the maximum safety limit [10]. Therefore, considering an effective battery thermal management system (BTMS) is crucial in EVs and HEVs.

Porous media and metal foams significantly enhance heat transfer, making them highly efficient for thermal management. The increased surface area offered by porous media facilitates more effective heat dissipation. The interconnected structure allows fluid flow, disrupting the thermal boundary layer and increasing the temperature gradient, thus boosting convective heat transfer. Using porous media also enhances heat transfer efficiency by leveraging high thermal conductivity [15–19]. Additionally, porous media provides uniform temperature distribution, and reducing hotspots which is crucial for BTMSs [20,21].

---

[*] Corresponding author.
E-mail address: noel.perera@bcu.ac.uk (N. Perera).

https://doi.org/10.1016/j.applthermaleng.2025.125848
Received 3 December 2024; Received in revised form 21 January 2025; Accepted 4 February 2025

Nomenclature

A_m	Mushy zone constant (kg· m^{-3}·s^{-1})
C	Inertial factor
C_0	Nominal capacity
C_F	Geometric function
C_p	Specific heat capacity (J·kg^{-1}·K^{-1})
D	Copper tube diameter (m)
E	Open circuit voltage (V)
E_d	Energy density (Wh·kg^{-1})
F	Faraday's constant (C·mol^{-1})
$\overrightarrow{F}$	Source term
F_s	Safety factor
f_r	Friction factor
I	Electric current (A)
K	Permeability of the porous medium (m^2)
L_b	Battery height (m)
L_f	Liquid fraction
N	Total number of grids
$\overline{Nu}$	Average Nusselt number
P	Pressure (Pa)
p	Rate of convergence
Q	Heat generation rate (W)
Re	Reynolds number
R_e	Total internal resistance (Ω)
$\overrightarrow{S}$	Source term
S_L	Source term
T	Temperature (K)
U	Nominal voltage
V	Voltage (V)
$\overrightarrow{V}$	Velocity vector (m·s^{-1})
V_b	Battery volume (m^3)
V_i	Volume of each grid cell (m^3)
a_{sf}	Specific surface area (m^{-1})
d_f	Ligament diameter (m)
d_p	Pore size (m)
f	Solution value
g	Gravitational acceleration (m·s^{-2})
h	Sensible enthalpy (J·kg^{-1})
h_f	Latent heat of fusion (J·kg^{-1})
h_{sf}	Solid-fluid heat transfer coefficient (W·m^{-2}·K^{-1})
k	Thermal conductivity (W·m^{-1}·K^{-1})
k_{td}	Thermal dispersion coefficient (W·m^{-1}·K^{-1})
n	Number of electrons
q_b	Heat generation per unit volume (W·m^{-3})
$q_{b,s}$	Heat flux on battery surface (W·m^{-2})
q_{int}	Heat flux at the interface (W·m^{-2})
r	Grid refinement ratio
t	Time (s)
ΔP	Pressure drop (Pa)
ΔS	Change in entropy (J·K^{-1})
ΔT	Temperature difference (K)
$\frac{dE}{dT}$	Entropy coefficient (V·K^{-1})

Greek letters

ω	Pore density (PPI)
β	Thermal expansion coefficient (K^{-1})
ε	Porosity
ε_r	Relative error
μ	Dynamic viscosity (Pa·s)
ρ	Density (kg·m^{-3})
θ	Dimensionless temperature

Subscripts

Max	Maximum
m	mean value
amb	Ambient
b	Battery
eff	Effective
f	Fluid phase
gen	Generated
irr	Irreversible
m	Melting
ref	Reference
rev	Reversible
s	Solid phase
t	Total

Acronyms

BTMS	Battery Thermal Management System
EV	Electric Vehicle
GCI	Grid Convergence Index
HBTMS	Hybrid Battery Thermal Management System
HEV	Hybrid Electric Vehicle
HPPC	Hybrid Pulse Power Characterization
LIB	Lithium-ion Battery
LTE	Local Thermal Equilibrium
LTNE	Local Thermal Non-Equilibrium
NMC	Lithium Nickel Manganese Cobalt Oxide
PCM	Phase Change Material
PEC	Performance evaluation criteria
PPI	Pores per inch
Sur	Surface
UDF	User Defined Function
r.e.v	Representative Elementary Volume

Integrating porous media and foams into hybrid battery thermal management systems (HBTMS) has shown promising results in improving the effectiveness of thermal management of batteries. Numerous investigations have shown that these hybrid systems are efficient at decreasing battery temperatures, enhancing temperature uniformity, and reducing power utilization. Yang et al. [22] numerically and experimentally investigated a hybrid cold plate configuration including water, RT35 paraffin wax, and aluminium foam for prismatic LIBs. The cooling method, which included periodically cycling the coolant at an increased flow rate and relying on latent heat of the phase change material (PCM), effectively decreased power usage by 90 % while ensuring battery temperatures remained below acceptable limits. Khaboshan et al. [23] conducted a numerical investigation on a HBTMS based on N-eicosane (PCM) within aluminium foam, and copper fins for 18,650 LIBs. Their research revealed that the battery surface temperature could be reduced by 3 K. The incorporation of fins served as a conduction network in the system, hence improving its overall thermal efficiency. Zhao et al. [24] performed an investigation on a hybrid system for 18,650 LIBs including water, paraffin, and copper foam. The obtained experimental and numerical results indicated that increased Reynold numbers (Re) came up with temperature non-uniformity, while the maximum battery temperature decreased. Liu et al. [25] conducted a numerical analysis on a HBTMS with 18,650 LIBs considering water, several kinds of PCMs (PCM28HC, PCM35HC, PCM44HC) and copper foam as composite PCM (CPCM). A reduction by almost 30 K was reported in battery surface temperature compared to natural convection. Also, flow velocity was emphasized as a notable parameter for lowering battery temperatures. Kiani et al. [26,27] performed experimental and

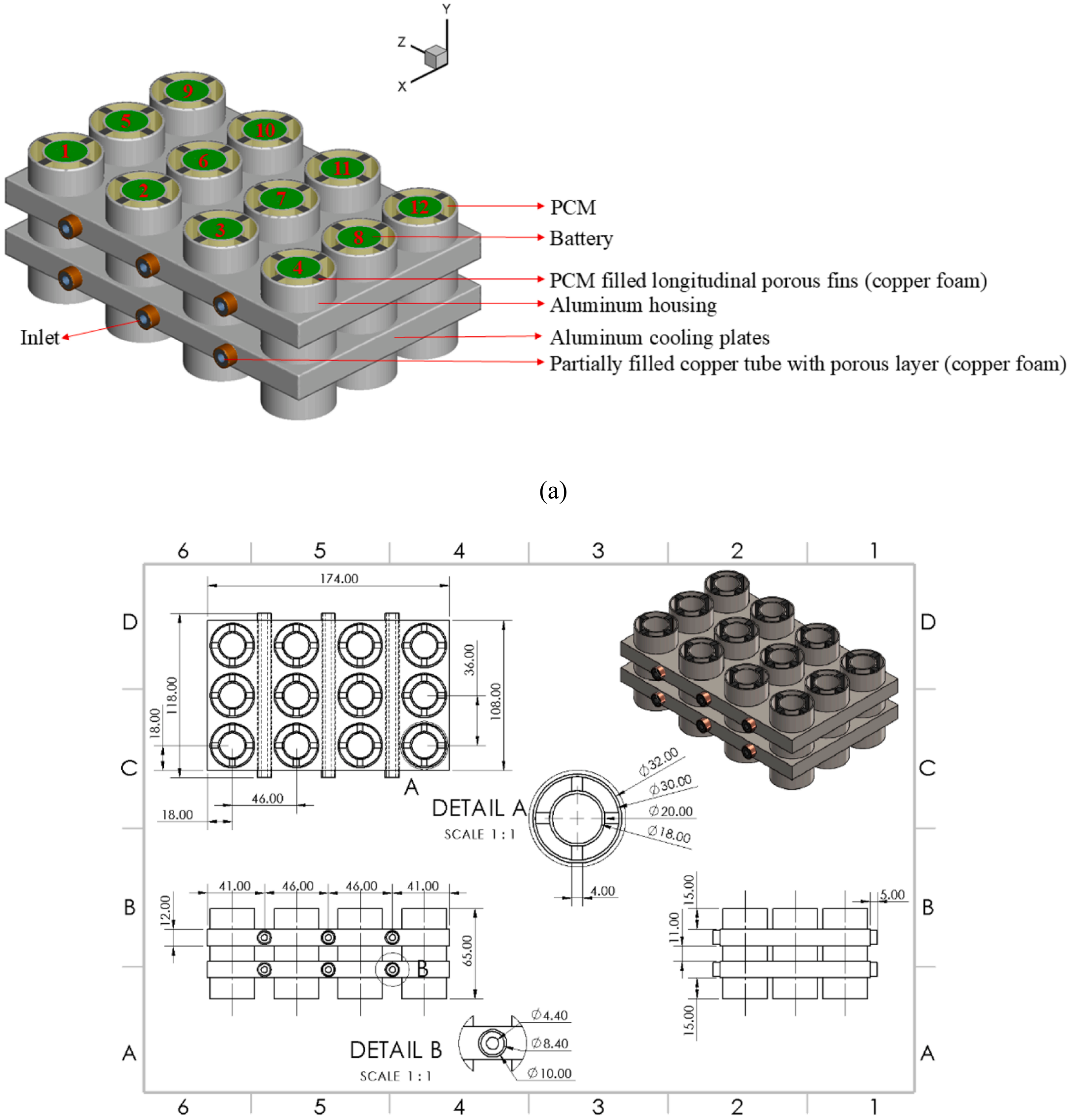

(a)

(b)

Fig. 1. The diagram of the proposed HBTMS (a) illustration of the different parts, and (b) dimensional details of the system.

numerical investigation on HBTMS based Al_2O_3-H_2O nanofluid, and paraffin wax within copper foam. Their study showcased that utilizing HBTMS in conjunction with a magnetic field resulted in a reduction of 22.5 % in the maximum temperature and a reduction of 79.3 % in the temperature difference, compared to systems using pure paraffin. Zhang et al. [28] experimentally investigated a HBTMS for prismatic $LiFePO_4$ batteries that integrated heat pipes, and paraffin within copper foam. The studied HBTMS effectively limited the highest temperature difference below 5 °C within the system, for high discharge rate of 5C. Also, a considerable reduction in temperature variations inside a single cell was reported, as compared to the baseline PCM-based BTMS. Li et al. [29] employed a combination of air, water, and paraffin within copper foam in their experimental and numerical investigation of HBTMS for 18,650 LIBs. They demonstrated that considering double-sided liquid cooling result in more effective temperature regulation, achieving the lowest battery temperature within the acceptable range when compared to single-sided and natural convection cooling. Rabiei et al. [30] performed a numerical investigation on cooling prismatic $LiFePO_4$ batteries using water and aluminium foam. The obtained results revealed that introduction of a wavy microchannel led to a substantial decrease of 50 % to 73 % in pumping power. In addition, considering the cooling channel entirely filled with metal foam increased the temperature difference, while effectively reduced the maximum temperature. Ki et al. [31] experimentally and numerically investigated a HBTMS for pouch-type LIBs by using water and aluminium foam layer. Maximum temperature of 43.3 °C and a temperature variation of less than 2 °C was achieved using a coolant flow rate of 3 L/min. The inclusion of a porous metal layer in the system improved heat transfer performance by increasing heat exchange surface area and reducing thermal resistance. Moaveni et al. [32] performed numerical simulations on a HBTMS incorporating nano-enhanced phase change materials (nano-PCM), fins, and metal foam to improve thermal performance of 18,650 LIBs. Their findings indicated significant reductions in peak battery temperatures, with the addition of nanoparticles and fins. Moreover, the obtained results revealed superior thermal regulation by the integration of copper foam with 0.9 porosity.

While numerous investigations have been conducted on the application of fins in BTMSs, particularly with PCM to enhance thermal

Table 1
Specification and thermophysical properties of the battery [43].

Parameter	Value
Nominal voltage (V)	3.7
Nominal capacity (Ah)	2.6
Cell mass (kg)	0.0475
Thermal conductivity in the radial direction ($W{\cdot}m^{-1}{\cdot}K^{-1}$)	0.2
Thermal conductivity in the axial direction ($W{\cdot}m^{-1}{\cdot}K^{-1}$)	37.6
Specific heat capacity ($J{\cdot}kg^{-1}{\cdot}K^{-1}$)	1200.0

Table 2
Thermophysical properties of the materials [34,44].

Materials	Properties	Value
Paraffin	Thermal conductivity ($W{\cdot}m^{-1}{\cdot}K^{-1}$)	0.2
Paraffin	Specific heat capacity ($J{\cdot}kg^{-1}{\cdot}K^{-1}$)	2000
Paraffin	Density ($kg{\cdot}m^{-3}$), solid	880
Paraffin	Density ($kg{\cdot}m^{-3}$), liquid	760
Paraffin	Solidus temperature (K)	311.15
Paraffin	Liquidus temperature (K)	316.15
Paraffin	Latent heat ($J{\cdot}kg^{-1}$)	174,000
Paraffin	Dynamic viscosity ($Kg{\cdot}m^{-1}{\cdot}s^{-1}$)	0.02
Paraffin	Thermal expansion coefficient (K^{-1})	0.0001
Al alloy	Thermal conductivity ($W{\cdot}m^{-1}{\cdot}K^{-1}$)	167
Al alloy	Specific heat capacity ($J{\cdot}kg^{-1}{\cdot}K^{-1}$)	896
Al alloy	Density ($kg{\cdot}m^{-3}$)	2700
Copper	Thermal conductivity ($W{\cdot}m^{-1}{\cdot}K^{-1}$)	387.6
Copper	Specific heat capacity ($J{\cdot}kg^{-1}{\cdot}K^{-1}$)	386
Copper	Density ($kg{\cdot}m^{-3}$)	8900
Water	Thermal conductivity ($W{\cdot}m^{-1}{\cdot}K^{-1}$)	0.6
Water	Specific heat capacity ($J{\cdot}kg^{-1}{\cdot}K^{-1}$)	4182
Water	Density ($kg{\cdot}m^{-3}$), solid	998.2
Water	Dynamic viscosity ($Kg{\cdot}m^{-1}{\cdot}s^{-1}$)	0.001003

conductivity [33–38], these studies primarily focus on conventional fin structures and their effects on heat transfer. The literature reveals a critical gap in exploring advanced fin designs, such as porous fins, and their integration with PCM in HBTMSs. The integration of porous fins offers unique advantages, including improved thermal performance, reduced system weight, and enhanced energy density compared to conventional solid fin, yet these benefits remain underexplored. Additionally, different investigations have been done on enhancement of liquid cooling in BTMSs using metal foam [30,31,39,40], but they have not fully optimised the potential of porous layers for liquid cooling in HBTMSs. Therefore, this study directly addresses these gaps by focusing on the optimisation of porous fin and layer properties such as porosity and pore density to achieve enhanced heat transfer and energy density in HBTMSs. The proposed HBTMS, illustrated in Fig. 1, represents a novel combination of passive cooling via porous fins with PCM and active cooling through liquid cooling with porous layer. By focusing on these underexplored aspects, this investigation aims to provide new insights into the effective utilization of porous media in HBTMSs, offering a comprehensive solution for enhancing both passive and active cooling mechanisms, while also improving the system's energy density.

2. Problem statement and description of the proposed HBTMS

The proposed HBTMS combines liquid cooling, PCM, and copper foam as porous fins and porous layers. As shown in Fig. 1, the battery pack consists of twelve Lithium-ion 18,650 batteries. Copper foam was used as longitudinal porous fins around the batteries in the PCM housing and as a porous layer within the copper tubes. Fig. 1(a) shows the different parts of the system. Each battery was placed in an aluminium housing to prevent direct contact with the PCM and ensure uniform heat transfer. Paraffin was used as the PCM and was filled into the PCM housing. To enhance the thermal conductivity of the PCM, longitudinal porous fins made of copper foam were added and the PCM was also considered within the pores of the porous fins. To control the phase change process of the paraffin, aluminium cooling plates with copper tubes passing through them were included, allowing water to serve as the liquid coolant in the system. Porous layers within the copper tubes enhance convection heat transfer, further improving the cooling efficiency. Fig. 1(b) provides detailed dimensions of the system, with dimensions selected based on common practice within the literature, manufacturing size limitations for copper foam, and manufacturing standards for copper tubes.

The selection of materials and design configurations in the HBTMS was driven by the need to balance thermal performance with system weight. Aluminium and copper foam were chosen for their excellent thermal properties and low density, contributing to an overall reduction in system weight and improved energy density. In the present investigation, a commercially available 18,650 lithium-ion battery ($LiNi_x Co_y Mn_z O_2$) or NCM has been considered due to its higher energy density. Also, NMC batteries are common in electric vehicles [41,42]. The specifications and thermophysical properties of the NMC 18650 LIB are shown in Table 1. To simplify the simulation model without compromising accuracy, the battery was considered as a homogenous cylinder. This approach was chosen since the detailed structure of a cylindrical battery has limited impact on its thermal performance [43]. The axial and radial thermal conductivities of the cylindrical lithium-ion battery change owing to differences in material compositions in various directions. Table 2 provides the thermophysical properties of the materials used in the study. The materials include aluminium alloy for the housings and cooling plates, copper foam as the porous fins and porous layers, and paraffin as PCM.

3. Numerical modelling

In order to investigate the influence of different parameters on the performance of the suggested HBTMS, 3D simulations were carried out using commercial CFD ANSYS FLUENT 23/R2 software. The HBTMS consists of 12 Lithium-ion 18,650 batteries, an aluminium housing, porous longitudinal fins, paraffin, an aluminium PCM housing, and aluminium cooling plates with copper tubes improved by porous layers.

3.1. 18,650 LIB transient heat generation

For realistic application scenarios, transient battery heat generation was considered. The lumped-capacitance model was used to simulate the actual transient heat generation of the lithium-ion battery, incorporating both resistive and entropic heat generation. To determine the suitability of the lumped-capacitance thermal model, the Biot number ($Bi = \frac{hL_b}{k_b}$) needs to be calculated. In this calculation, h is the convective heat transfer coefficient, L_b is the characteristic length derived from the ratio of the battery's volume to its surface area, and k_b is the thermal conductivity of the battery. The lumped-capacitance thermal model is applicable when the Biot number is low, typically less than 0.1 [45]. In this model, the battery is assumed to have constant thermo-physical properties throughout, with heat generation dependent on voltage and current characteristics [46]. The total heat generation of lithium-ion batteries is mathematically described by the Bernardi equation [43]:

$$Q_t = Q_{irr} + Q_{rev} \tag{1}$$

$$Q_{irr} = I(E - V) = I^2 R_e \tag{2}$$

$$Q_{rev} = -T\Delta S\left(\frac{I}{nF}\right) = -I\left[T\left(\frac{dE}{dT}\right)\right] \tag{3}$$

where the total heat generation in the battery Q_t is identified along with irreversible heat Q_{irr}, reversible heat Q_{rev}, open circuit voltage E, terminal voltage V, electric current I, temperature T, total internal resistance R_e, change in entropy ΔS, number of electrons n, Faraday's constant F, and the entropy coefficient $\frac{dE}{dT}$. Hybrid Pulse Power

Characterization (HPPC) test [47] is commonly used to develop functions for the total internal resistance and the entropy coefficient. The experimental data provided by [43,48,49] has been used with the above equations to model transient heat generation for discharge rates of 1C, 3C, and 5C. The discharge rate, or C-rate, is defined as the discharge current divided by the battery's nominal capacity [50]. Therefore, discharge time for discharge rates of 1C, 3C, and 5C is 3600, 1200, and 720 s, respectively. Transient heat generation equations have been added as User Defined Function (UDF). The heat generation per unit of the battery volume (V_b) is defined as follows:

$$q_b = \frac{Q_t}{V_b} \tag{4}$$

3.2. Governing equations

The enthalpy-porosity model was employed to simulate PCM, where the mushy zone (where solid and liquid phases coexist) is treated as a porous medium. This model integrates latent heat effects into the energy equation, avoiding explicit tracking of the phase interface [51,52]. During the melting/solidification process, a pure phase change material (PCM) without copper foam comprises three distinct zones: the solid zone, the liquid zone, and the mushy zone. In the mushy zone, the pure PCM is modelled as a porous material where unmelted PCM forms the solid matrix, and melted PCM fills the pores as the liquid component. Conversely, when simulating a composite PCM embedded with copper foam, the liquid zone is also treated as a porous medium but with a porosity distinct from that of the mushy zone [53].

To model copper foam as porous media, the Darcy-Brinkman-Forchheimer (DBF) model has been utilized. Local thermal equilibrium (LTE) model was applied to the porous fins, while local thermal non-equilibrium (LTNE) model was used for the porous layer within the copper tube.

To simplify the present numerical simulations the following assumptions were made:

- The laminar flow of molten PCM is unsteady and incompressible.
- PCM phases are isotropic and homogeneous.
- The liquid PCM and water are Newtonian fluid.
- The Boussinesq approximation has been used to account for buoyancy forces in natural convection.
- Changes in volume during the PCM melting process and effects of viscous dissipation and radiation are negligible.
- The influence of thermal resistance between the zones' surfaces has been ignored.
- The copper foam structure is assumed to be homogeneous and isotropic.
- Thermal equilibrium is considered between PCM and porous fins.
- Thermal non equilibrium is considered between water and porous layers.

Considering the mentioned assumptions the governing equations for PCM and porous fins are as follows [54]:

Continuity:

$$\frac{\partial \rho_f}{\partial t} + \nabla . \rho_f \overrightarrow{V} = 0 \tag{5}$$

Momentum:

$$\frac{\rho_f}{\varepsilon}\frac{\partial \overrightarrow{V}}{\partial t} + \frac{\rho_f}{\varepsilon^2}\left(\overrightarrow{V}.\nabla\right)\overrightarrow{V} = -\nabla P + \frac{\mu_f}{\varepsilon}\left(\nabla^2 \overrightarrow{V}\right) - \rho_{f,ref}\beta_f\varepsilon\left(T - T_{ref}\right)\overrightarrow{g} - \overrightarrow{S} - \overrightarrow{F} \tag{6}$$

where ρ is the density, ε is the porosity, $\overrightarrow{V}$ is the velocity vector, P is the pressure, μ is the dynamic viscosity, β is the thermal expansion coefficient, T is temperature, and $\overrightarrow{g}$ is the gravitational acceleration.

The source terms in the momentum equation account for the pressure loss caused by the melting process and are defined by Darcy's law of damping as follows [54]:

$$\overrightarrow{S} = A_m \frac{(1 - L_f)^2}{{L_f}^3 + 0.001}\overrightarrow{V} \tag{7}$$

where A_m is the mushy zone constant that has been considered to be 10^5 [44] and L_f is the liquid fraction.

In the governing equations for the PCM-only case or the regions that are not occupied by porous fins, the porosity is equal to 1, and the momentum equation lacks the source terms due to the absence of porous media. Additionally, L_f is defined as follows [55]:

$$L_f = \frac{\Delta H}{L_f} = \begin{cases} 0 if T < T_s \\ \frac{T - T_{Solidus}}{T_{Liquidus} - T_{Solidus}} T_s \leq T \leq T_l \\ 1 if T > T_l \end{cases} \tag{8}$$

where ΔH is latent heat.

The total enthalpy is calculated as follows:

$$H = h + \Delta H \tag{9}$$

where h is the sensible enthalpy and defined as:

$$h = h_{ref} + \int_{T_{ref}}^{T} C_{p_f} dT \tag{10}$$

where h_{ref} is sensible enthalpy at reference temperature and C_p is the specific heat.

The last term on the right-hand side of the momentum equation, which is caused by the porous medium, is defined as:

$$\overrightarrow{F} = \left(\frac{\mu_f}{K} + \frac{\rho_f C\left|\overrightarrow{V}\right|}{\sqrt{K}}\right)\overrightarrow{V} \tag{11}$$

where $\left|\overrightarrow{V}\right|$ is the magnitude of the velocity vector. In the above equations, the first term represents the viscous loss, and the second term represents the inertial loss. In these equations, K and C are permeability and inertial factor, respectively, and are given as [56]:

$$K = 0.00073(1 - \varepsilon)^{-0.224}{d_f}^{-1.11}{d_p}^{3.11} \tag{12}$$

$$C = 0.0012(1 - \varepsilon)^{-0.132}\left(\frac{d_f}{d_p}\right)^{-1.63} \tag{13}$$

where d_f and d_p are ligament diameter, pore size, respectively. They are defined as follows [57,58]:

$$d_f = 1.18 d_p \sqrt{\frac{1 - \varepsilon}{3\pi}} \tag{14}$$

$$d_p = 0.0224/\omega \tag{15}$$

where ω is the pore density as pores per inch (PPI).

Energy:

By considering LTE model, in which the PCM and porous fins are assumed to have the same temperature, the energy equation is given as [54]:

$$\frac{\partial \varepsilon \rho_f C_{p_f} T}{\partial t} + \nabla\left(\rho_f C_{p_f}\overrightarrow{V}.T\right) = \nabla(k_{eff}\nabla T) - S_L \tag{16}$$

where k_{eff} is the effective thermal conductivity and defined as follows [59]:

$$k_{eff} = (1 - \varepsilon)k_s + \varepsilon k_f \tag{17}$$

Table 3
GCI analysis for different studied grids.

Grid number (N)	h_i	r	(f_i) $T_{sur,\ max}$ (K)	ε_r	GCI (%)
4,944,155	1	1.25	313.894287	0.052741	18.30
6,612,690	0.8	1.25	313.897891	0.003603	1.25
11,642,045	0.64	–	313.845152	–	–

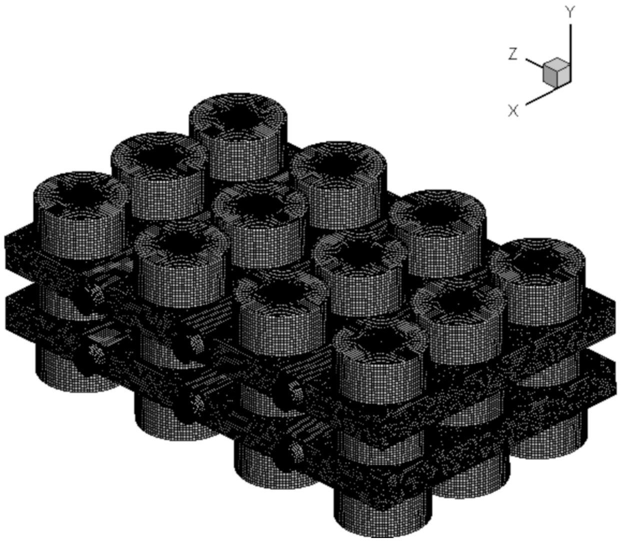

Fig. 2. Generated mesh for the HBTMS.

Table 4
Different time steps for time step independency study.

Time step	$T_{sur,\ max}$ (K)	Error (%)
0.25	313.9788	–
0.5	313.9391	0.012635
1	313.8943	0.014271
2	313.7315	0.051876

where k is the thermal conductivity.

The last source term in the energy equation is defined as follows [60]:

$$S_L = \frac{\partial \varepsilon \rho_f L_f h_f}{\partial t} + \nabla\left(\rho_f \overrightarrow{V}.T\lambda h_f\right) \tag{18}$$

where h_f is the latent heat of fusion.

The governing equations for liquid cooling with porous layer by considering LTNE model, are as follows [61,62]:

Continuity:

$$\frac{\partial \rho}{\partial t} + \nabla.\rho\overrightarrow{V} = 0 \tag{19}$$

Momentum:

Clear region:

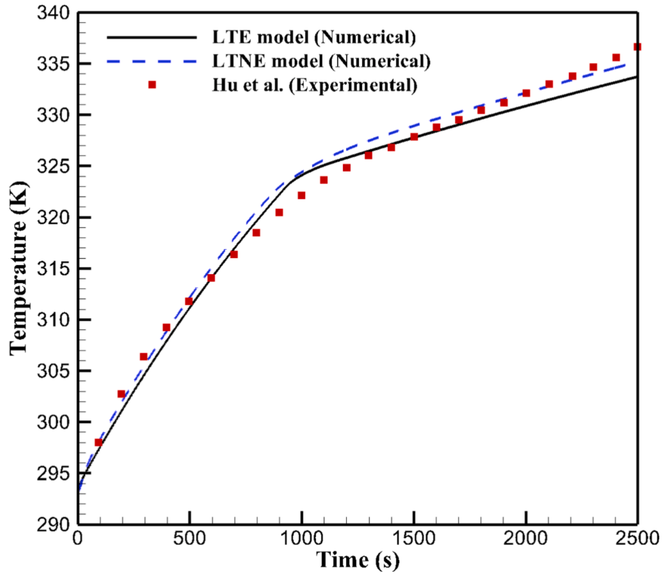

Fig. 4. Comparison of the present numerical results with experimental investigation of Hu et al. [74].

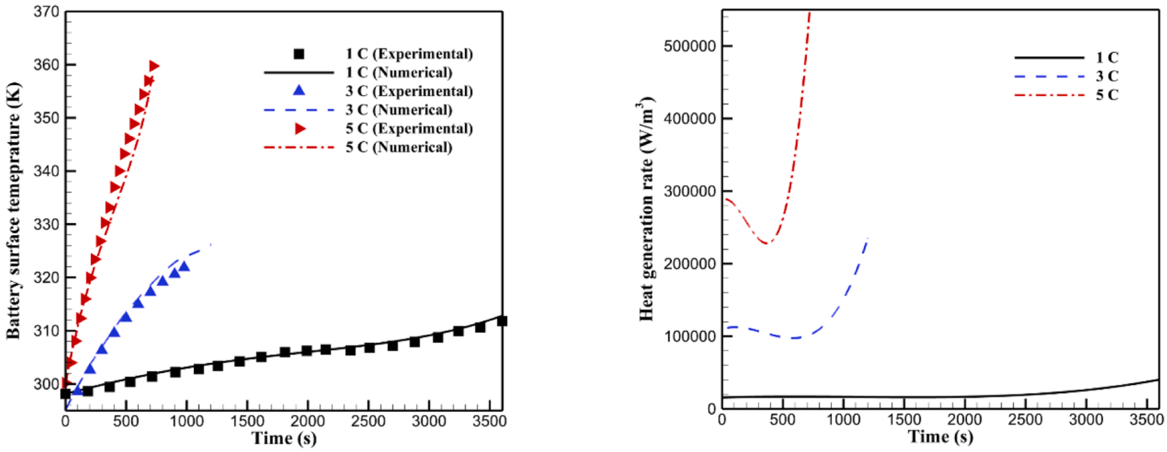

a)   (b)

Fig. 3. Comparison of battery performance (a) present numerical and experimental surface temperatures and (b) volumetric heat generation at various discharge rates.

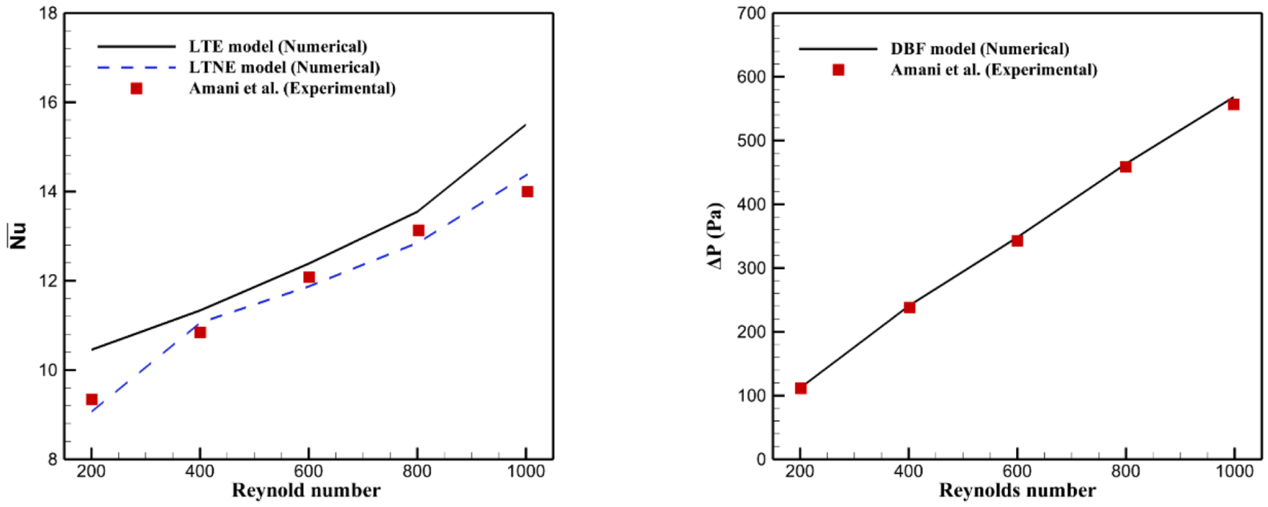

(a) (b)

Fig. 5. Comparison of the current numerical results with the experimental investigation by Amani et al. [75] for (a) average Nusselt number and (b) pressure drop.

$$\rho\frac{\partial\vec{V}}{\partial t}+\rho\nabla.\left(\vec{V}\vec{V}\right)=-\nabla P+\mu_f\left(\nabla^2\vec{V}\right)\tag{20}$$

Porous region:

$$\rho\frac{\partial\vec{V}}{\partial t}+\frac{\rho}{\varepsilon}\nabla.\left(\vec{V}\vec{V}\right)=-\nabla P+\mu_f\left(\nabla^2\vec{V}\right)-\frac{\mu_f\vec{V}}{K}-\rho C_F\sqrt{\frac{1}{K}}\left|\vec{V}\right|\vec{V}\tag{21}$$

where C_F and K are the permeability of the porous media and the geometric function, respectively and can be expressed as [63]:

$$K=\frac{\varepsilon^3 d_p^2}{150(1-\varepsilon)^2}\tag{22}$$

$$C_F=\frac{1.75}{\sqrt{150}\varepsilon^{3/2}}\tag{23}$$

Energy:

Clear region:

$$\frac{\partial\left(\rho C_p T_f\right)}{\partial t}+\nabla\cdot\left(\rho C_p\vec{V}T_f\right)=\nabla\cdot\left(k_f\nabla T_f\right)\tag{24}$$

Porous region:

Solid phase:

$$\frac{\partial\left(\rho_s C_p T_s\right)}{\partial t}=\nabla\cdot\left(k_{s_{eff}}\nabla T_s\right)-h_{sf}a_{sf}\left(T_s-T_f\right)\tag{25}$$

Fluid phase:

$$\frac{\partial\left(\rho_f C_p T_f\right)}{\partial t}+\nabla\cdot\left(\frac{\rho_f C_p\vec{V}T_f}{\varepsilon}\right)=\nabla\cdot\left(k_{f_{eff}}\nabla T_f\right)+h_{sf}a_{sf}\left(T_s-T_f\right)\tag{26}$$

where $k_{s_{eff}}$ and $k_{f_{eff}}$ are effective thermal conductivity for solid and porous phase of the porous media, respectively, and defined as follows [64–66]:

$$k_{s_{eff}}=(1-\varepsilon)^{0.763}k_s\tag{27}$$

$$k_{f_{eff}}=\varepsilon k_f+k_{td}\tag{28}$$

where k_{td} is the thermal dispersion coefficient which is calculated as follows:

$$k_{td}=0.025\rho_f C_p\sqrt{K}\left|\vec{V}\right|\tag{29}$$

h_{sf} and a_{sf} appearing in the energy equation are fluid-to-solid heat transfer coefficient and specific surface area [67,68]:

$$h_{sf}=\left(\frac{k_f}{d_p}\right)^2\left(1+1.1\left(\frac{C_{p_f}\mu_f}{k_f}\right)^{1/3}\right)\left(\frac{\rho_f\left|\vec{V}\right|d_p}{\mu_f}\right)^{0.6}\tag{30}$$

$$a_{sf}=\frac{6(1-\varepsilon)}{d_p}\tag{31}$$

Battery cell:

$$\rho_b c_{p_b}\frac{\partial T}{\partial t}=\nabla\cdot(k_b\nabla T)+\dot{Q}_{gen}\tag{32}$$

Cooling plates:

$$\rho_s c_{p_s}\frac{\partial T}{\partial t}=\nabla\cdot(k_s\nabla T)\tag{33}$$

3.3. Initial and boundary conditions

The initial condition for the simulation of the HBTMS was set as follows:

$$T(x,y,z)=T_{amb};t=0\tag{34}$$

where T_{amb} is the ambient temperature, which was assumed to be 308.15 K for simulations.

The adiabatic boundary condition has been considered at the bottom surface of the HBTMS. Mass flow inlet boundary condition, with constant value of 0.001 kg/s, has been assumed at the water inlet, with a temperature of 303.15 K, into the copper tubes with porous layers. Additionally, based on the dimensions provided in Fig. 1(b) and the thermophysical properties of the materials listed in Table 2, the Reynolds number in the clear region of the copper tube was calculated to be 151.2, which is well below the critical threshold of 2000. Similarly, the permeability Reynolds number [69] for the porous layer was determined to be 0.123, which is significantly below the threshold value of 100 [15]

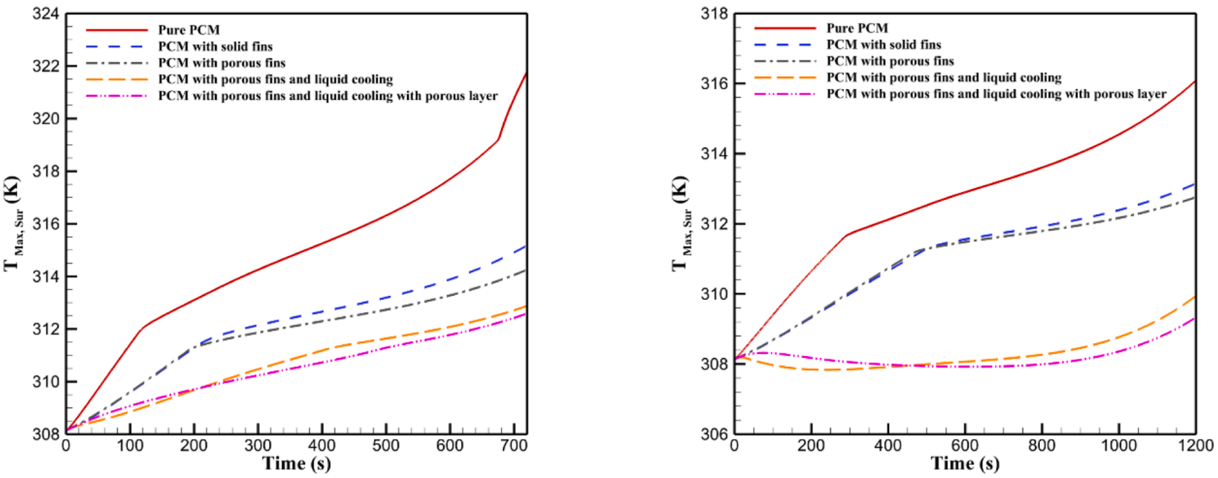

(a) 5C (b) 3C

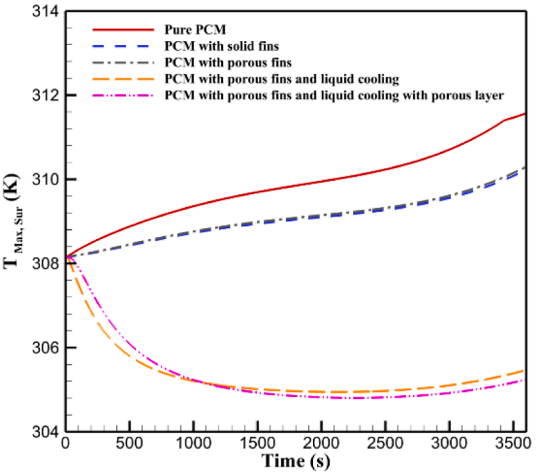

(c) 1C

Fig. 6. Maximum battery surface temperature for different BTMS under various battery discharge rates.

for turbulent flow in porous media. Therefore, the assumption of laminar flow has been consistently applied to all simulations. At the outlet, pressure outlet boundary condition has been set at the atmospheric pressure. No slip boundary condition was adopted at the walls. On the other surfaces of the HBTMS natural boundary condition has been assumed as follows:

$$-k_{wall}\frac{\partial T_{wall}}{\partial n}=h(T_{wall}-T_{amb}) \tag{35}$$

where h is the convection heat transfer coefficient and was considered to be 10 W·m^{-2}·K^{-1} [50] for air natural convection.

At the interface between solid and liquid phase of the porous media the following boundary conditions were considered for LTE and LTNE models.

LTE model [19]:

$$\vec{V}\Big|_{fluid}=\vec{V}\Big|_{porous} \tag{36}$$

$$\mu_f\frac{\partial\vec{V}}{\partial n}\Big|_{fluid}=\mu_{eff}\frac{\partial\vec{V}}{\partial n}\Big|_{porous}$$

$$T_{fluid}=T_{porous},$$

$$k_f\frac{\partial T}{\partial n}\Big|_{fluid}=k_{eff}\frac{\partial T}{\partial n}\Big|_{porous}$$

LTNE model [70]:

$$\vec{V}\Big|_{fluid}=\vec{V}\Big|_{porous} \tag{37}$$

$$\mu_f\frac{\partial\vec{V}}{\partial n}\Big|_{fluid}=\mu_{eff}\frac{\partial\vec{V}}{\partial n}\Big|_{porous}$$

$$-k_f\frac{\partial T}{\partial n}\Big|_{fluid}=-k_{s_{eff}}\frac{\partial T}{\partial n}\Big|_{porous}=q_{interface}$$

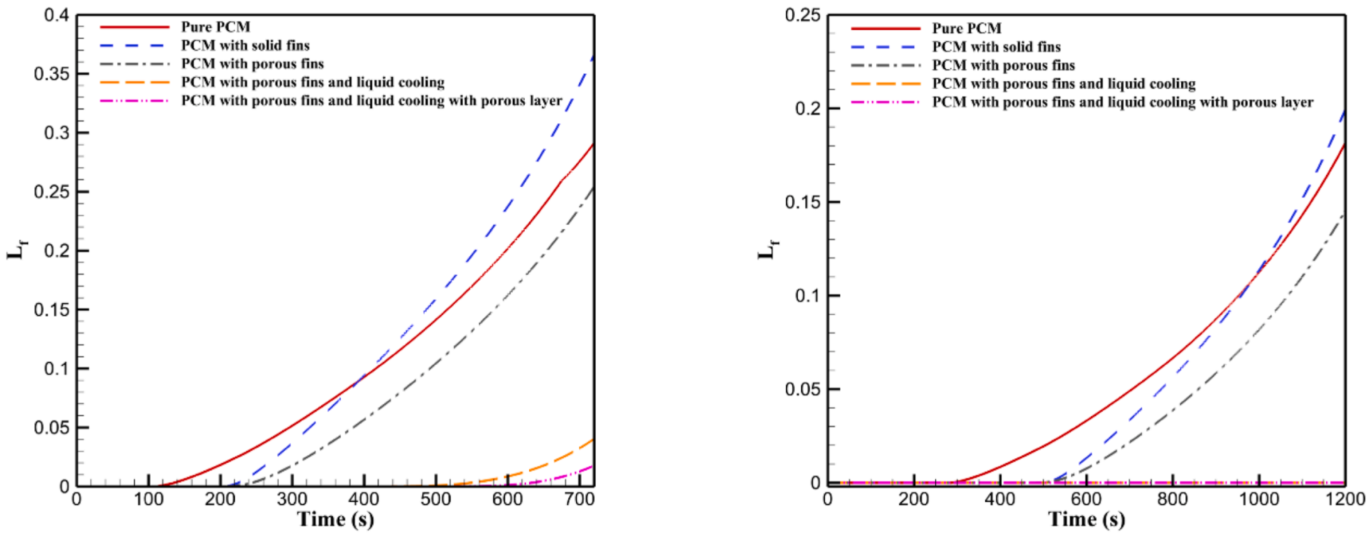

(a) 5C

(b) 3C

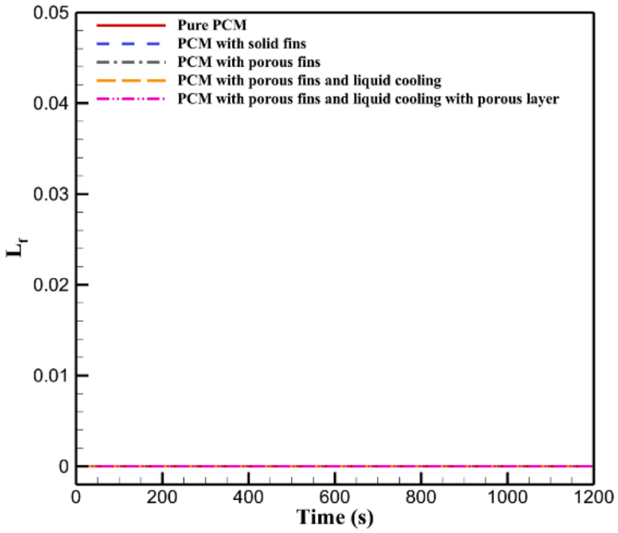

(c) 1C

Fig. 7. PCM liquid fraction for different BTMS under various battery discharge rates.

$$-k_f\frac{\partial T}{\partial n}\bigg|_{fluid} = -k_{f_{eff}}\frac{\partial T}{\partial n}\bigg|_{porous} = q_{interface}$$

The governing equations were solved numerically incorporating mentioned initial and boundary conditions. The SIMPLE scheme was employed for pressure–velocity coupling. To discretize the equations, the second-order upwind scheme was applied. The representative elementary volume (r.e.v.) method was used to model the porous media. The enthalpy-porosity model was applied to simulate the PCM phase change. The convergence criteria for the residuals were set at 10^{-4} for the continuity and momentum equations, and 10^{-6} for the energy equation.

3.4. Validation, mesh independence, and time-step independence studies

The grid independence was assessed using the Grid Convergence Index (GCI) [71,72]. The GCI for the computational grid is defined as follows:

$$GCI = F_s\frac{|\varepsilon_r|}{r^p - 1} \tag{38}$$

where F_s is a safety factor, the value is 1.25 for three grids comparisons. p is the rate of convergence, the theoretical value is 1.97 for a second-order method. The relative error ε_r is defined as:

$$\varepsilon_r = \frac{f_{i+1} - f_i}{f_i} \tag{39}$$

where $f_{\mathrm{i+1}}$ and f_{i} are the solution values on the fine and coarse grids, respectively. In this context, these values represent the maximum temperature of the battery surface at the end of 5C discharge. The grid refinement ratio r_i is defined as:

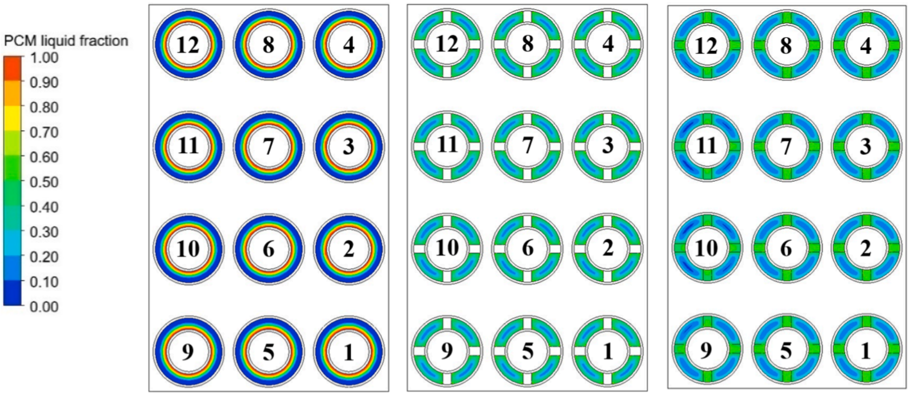

(a) Pure PCM (b) PCM with solid fins (c) PCM with porous fins

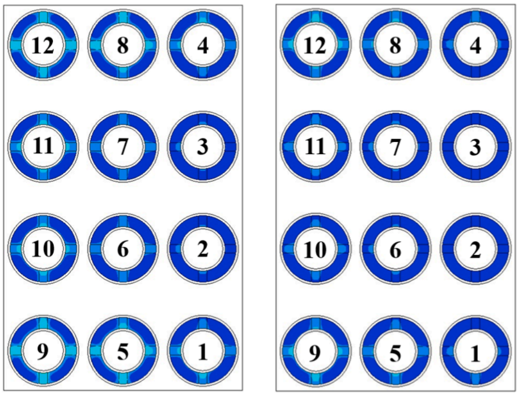

(d) PCM with porous fins and liquid cooling (e) PCM with porous fins and liquid cooling with porous layer

Fig. 8. PCM liquid fraction contour plots for different BTMS at the end of the 5C discharge rate.

$$r_{i,i+1} = \frac{h_i}{h_{i+1}} \tag{40}$$

$$h_i = \sqrt[3]{\frac{\sum_{i-1}^{N} \Delta V_i}{N}} \tag{41}$$

where h_i represents the average grid spacing, V_i denotes the volume of each grid cell, and N stands for the total number of grids.

Three types of grid densities and their corresponding GCI calculations are presented in Table 3. The GCI for 6,612,690 grid cells is below 3 % which meets the grid convergence index criterion [73]. Also, the generated mesh for the HBTMS is shown in Fig. 2.

Different time steps were studied to check time step independencies. Table 4 provides the maximum temperature of the battery surface at the end of 5C discharge for different time steps. As shown, a time step of 1 s was found to be appropriate for the current investigation.

The numerical methods employed in this study were validated against various experimental investigations. To validate the Bernardi model used for transient battery heat generation, the battery surface temperatures were compared with experimental data from [43,48,49]. The comparisons are presented in Fig. 3(a). Also, the transient volumetric heat generation rate of the battery at various discharge rates is illustrated in Fig. 3(b). To model porous media, the commonly used methods of local thermal equilibrium (LTE) and local thermal non-equilibrium (LTNE) were both validated. For the application of longitudinal porous fins in phase change materials (PCM), the experimental study by Hu et al. [74] was considered, which involved aluminium foam filled with paraffin. The experimental temperature data were compared with the numerical results obtained using both LTE and LTNE methods, as shown in Fig. 4. Both models accurately predicted the temperature of the composite PCM; however, the LTNE model demonstrated even higher accuracy. Despite this, due to the similar results from both models and the reduced computational time required by the LTE model, the LTE method was ultimately chosen for the simulations of porous fins.

To validate the insertion of porous layers into copper tubes, the experimental study by Amani et al. [75] was simulated. This investigation involved water flow through a copper tube filled with copper foam. The numerical results for the average Nusselt number on the tube surface and the pressure drop were compared with the experimental data, as shown in Fig. 5. When considering both the LTE and LTNE models, the LTNE model proved to be more accurate. Therefore, the LTNE model was chosen for the simulation of porous layer in the copper tube. The simulation results for various scenarios closely align with the experimental data, affirming the precision and reliability of the findings.

4. Results and discussion

In this section, the proposed HBTMS has been compared in detail with PCM based BTMSs in terms of different design and performance criteria. Also, the impact of porous fins and porous layers' porosity and pore density have been investigated.

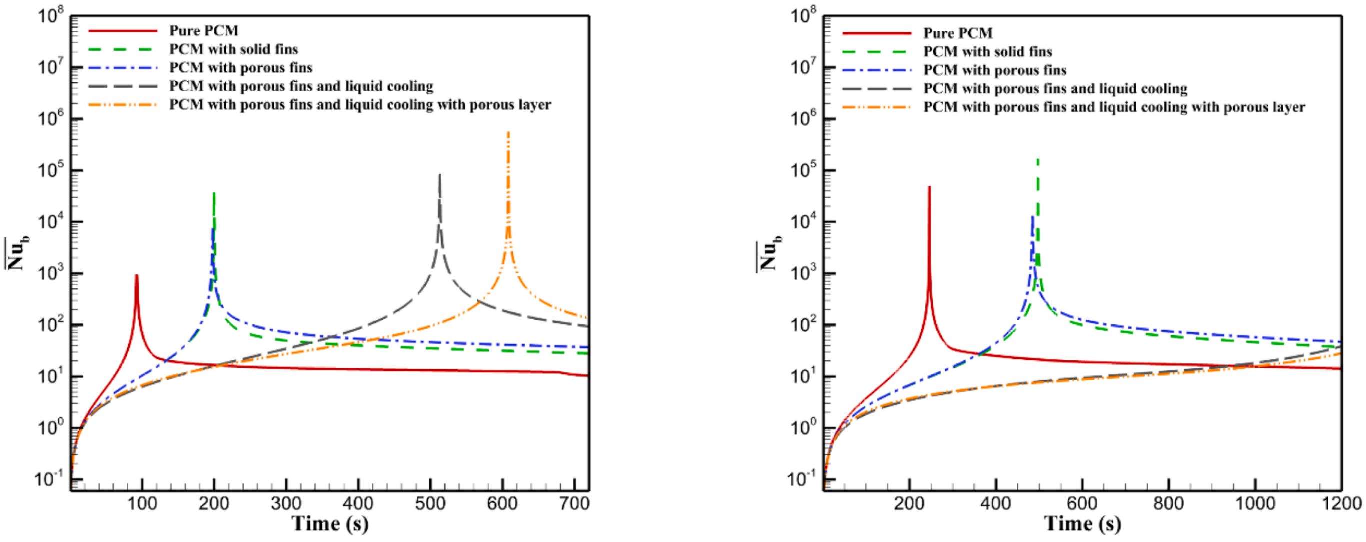

(a) 5C

(b) 3C

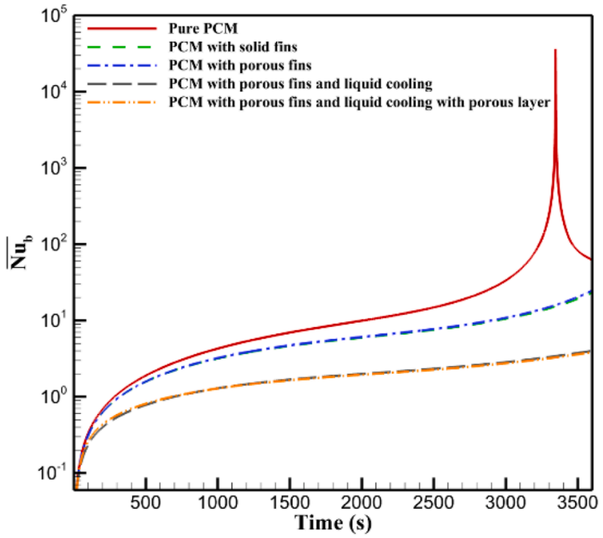

(c) 1C

Fig. 9. Average Nusselt number on batteries surface for different BTMS under various battery discharge rates.

4.1. Comparison of the proposed HBTMS with PCM based BTMSs

The effectiveness of the proposed HBTMS, PCM with porous fins and liquid cooling with porous layers, was investigated under different discharge rates. The performance of the HBTMS was compared with various BTMS configurations, including pure PCM, PCM with solid fins, PCM with porous fins, and PCM with porous fins combined with liquid cooling. Transient heat generation of 18,650 lithium-ion batteries was analysed at discharge rates of 1C, 3C, and 5C. The porosity and pore density of the porous layers and porous fins were set at constant values of 0.9 and 30 PPI, respectively.

To highlight the novelty of the HBTMS, the application of novel porous fins is first compared with pure PCM and PCM with solid fins (In Figs. 6–12). Subsequently, liquid cooling, both without and with a porous layer within the copper tube, is compared with pure PCM BTMS (In Figs. 6–12).

As depicted in Fig. 6, the maximum battery surface temperature ($T_{Max,\ Sur}$) for the pure PCM BTMS increases rapidly at the highest discharge rate, progressing through three distinct phases: before reaching the PCM solidus temperature (311.15 K), between the solidus and liquidus temperatures (316.15 K), and beyond. These stages correspond to different heat storage phases within the PCM: sensible heat storage prior to the phase change, latent heat storage during the phase transition, and continued sensible heat storage after the PCM has completely melted. A similar temperature increase was observed at lower discharge rates, though only two phases of temperature rise were noted, as temperatures did not reach the PCM's liquidus point. This phenomenon is attributed to the low thermal conductivity of pure PCM. As can be seen in Fig. 7, for different discharge rates, more PCM melts in pure PCM BTMS compared to other configurations, with melting

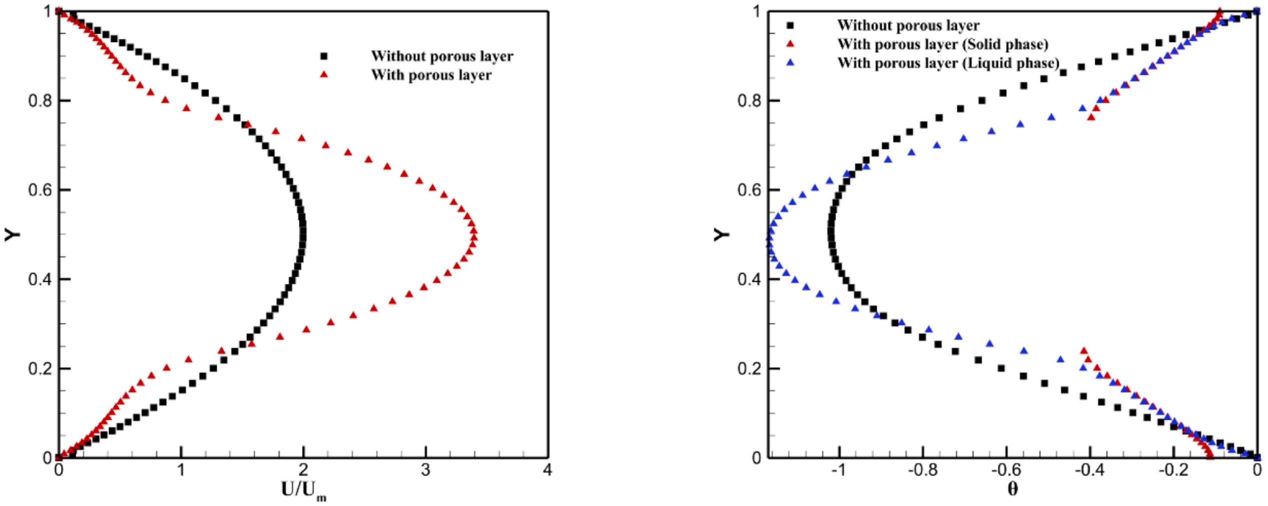

(a)

(b)

Fig. 10. Comparison of dimensionless (a) velocity and (b) temperature at the middle of the copper tube along the vertical axis with and without porous layer at the end of 5C discharge rate.

commencing nearly at the start of the discharge. Furthermore, contour plots of the PCM liquid fraction in Fig. 8(a) reveal that at the end of the 5C discharge, the heat generated by the battery was primarily dissipated within the pure PCM through conduction and its sensible heat capacity. Due to the low thermal conductivity of pure PCM, most of the heat was utilized in melting the PCM near the battery housing surface, forming a thin layer of molten PCM around the housing. Due to the poor thermal conductivity of this melted layer, it acts as insulation, hindering efficient heat dissipation. These observations underscore the need for the development of HBTMS, which integrates PCM, as pure PCM alone may not sufficiently maintain battery temperatures within safe limits during prolonged usage or at higher discharge rates.

As the primary criterion for evaluating the proposed HBTMS, $T_{Max,\ Sur}$ and PCM liquid fraction were considered. As shown in Fig. 6, adding fins, whether conventional longitudinal solid fins or innovative porous fins, significantly impacts $T_{Max,\ Sur}$ at different discharge rates. Considering pure PCM BTMS as a baseline, the maximum surface temperature reaches 321.77 K, 316.08 K, and 311.57 K at the end of discharge rates of 5C, 3C, and 1C, respectively. By adding solid fins to the PCM, the $T_{Max,\ Sur}$ is reduced by 6.6 K, 2.94 K, and 1.27 K for discharge rates of 5C, 3C, and 1C, respectively. Further reduction was observed with PCM incorporating porous fins, resulting in a drop of 7.52 K, 3.33 K, and 1.34 K for discharge rates of 5C, 3C, and 1C, respectively. The generated heat by the battery is transferred via conduction through the aluminium battery housing to the PCM and further conducted within the PCM to the housing in the HBTMS. The enhancement is attributed to the addition of fins, which improves heat conduction by forming conduction paths within the PCM. In addition, the presence of fins significantly influences the extent and area of PCM melting. As shown in Fig. 7, the volume average PCM liquid fraction (L_f) value is markedly affected by fins, with both types of fins causing a similar delay in the onset of PCM melting. At the end of the 5C discharge rate, L_f for pure PCM reached nearly 0.3. However, the inclusion of solid fins increases the L_f value by 24 %, raising it to 0.36 due to improved conduction compared to pure PCM. Conversely, porous fins within PCM decrease the amount of melted PCM by 14 %, reducing L_f to 0.25. A similar pattern was observed for the 3C discharge rate in Fig. 7 (b), with less PCM melting due to lower transient heat generation. Nonetheless, at a 1C discharge rate, all the heat generated by the batteries was absorbed as sensible heat storage, preventing phase change from occurring.

When comparing the heat transfer mechanisms for solid and porous fins, the solid fins transfer the battery's generated heat through conduction to the housing, and a similar mechanism occurs in porous fins. However, as the PCM begins to melt within the pores of the porous fins, natural convection is introduced in addition to conduction. The pores in the porous fins facilitate fluid movement as the PCM melts, enhancing heat transfer throughout the PCM by mixing and circulating it internally. Moreover, the porous structure increases the surface area available for heat transfer compared to solid fins. Therefore, as shown in Fig. 6 (a) and (b), both types of fins provide almost the same maximum surface temperature for the battery just before the PCM melting onset, occurring at 200 s and 480 s for 5C and 3C discharge rates, respectively. After this point, better heat transfer performance was observed for porous fins.

As illustrated in the PCM liquid fraction contours in Fig. 8 (a), (b), and (c), less PCM was melted near the battery housing when using configurations other than pure PCM. For solid fins, heat transfer occurs mainly through conduction, leading to localized heating around the fins and increased PCM melting in these areas and around the PCM housing. In contrast, with porous fins, PCM melting predominantly occurs within the porous fins and PCM housing. The porous fins provide nucleation sites for the phase change, potentially resulting in a more uniform melting within the pores. Thus, the enhanced heat transfer observed in porous fins can be attributed to the combined effects of increased surface area, enhanced convection due to liquid PCM movement within the pores, and improved heat distribution throughout the PCM.

The enhanced heat transfer performance of the HBTMS was reflected in the average Nusselt number on the battery's surface. The average Nusselt number on the battery surface is defined as follows [76]:

$$\overline{Nu}_b = \frac{q_{b,s}L_b}{\left(T_{b,sur} - T_{PCM,m}\right)K_{l,PCM}} \tag{42}$$

where $q_{b,s}$, L_b, $T_{b,sur}$, $T_{PCM,m}$, $K_{l,PCM}$ are heat flux on the battery surface, battery height, battery surface temperature, PCM melting temperature, and liquid PCM thermal conductivity, respectively.

Heat transfer enhancement was compared based on the average Nusselt number, as depicted in Fig. 9. For different types of BTMS, the Nusselt number increased significantly until melting commenced and

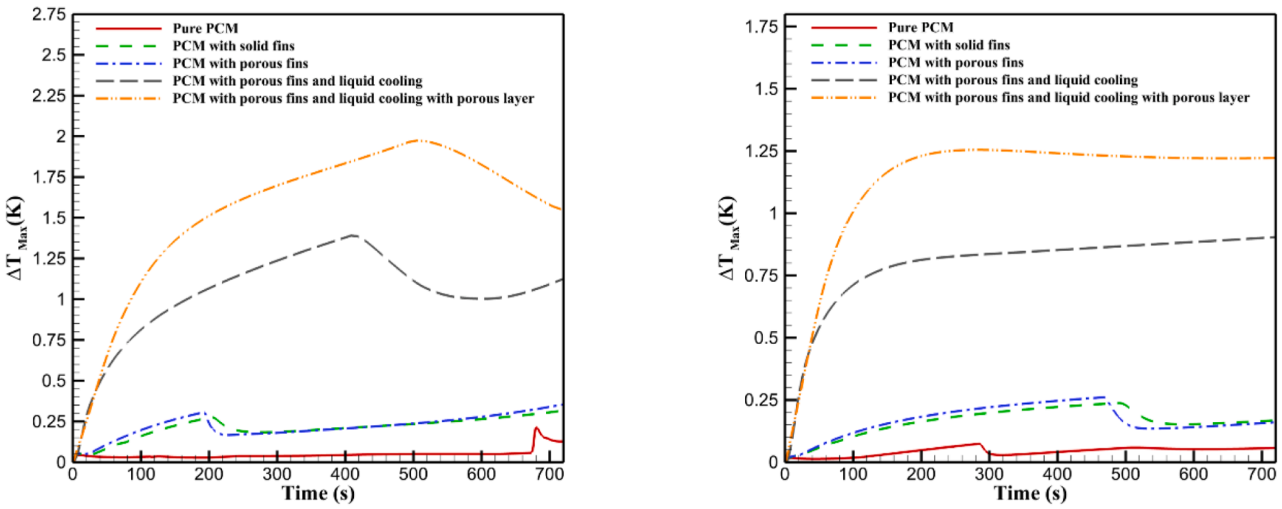

(a) 5C

(b) 3C

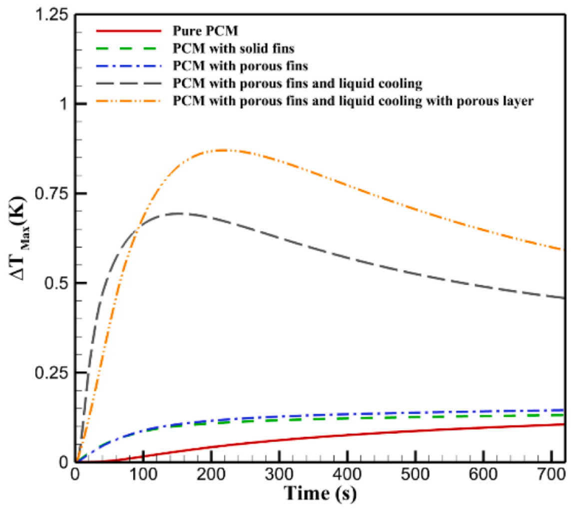

(c) 1C

Fig. 11. Maximum temperature difference within the battery pack for different BTMS under various battery discharge rates.

the surface temperature exceeded the PCM solidus temperature. Subsequently, the Nusselt number gradually declined until the completion of the discharge. Unlike the 1C discharge rate, where the PCM did not melt, higher discharge rates of 3C and 5C showed a higher average Nusselt number for both solid and porous fins compared to pure PCM after melting. At the end of the 5C discharge rate, the average Nusselt number improved by 172 % and 260 % for solid and porous fins, respectively. For the 3C discharge rate, the average Nusselt number was enhanced by 161 % and 231 % for solid and porous fins, respectively. However, as shown in Fig. 9(c), during the 1C discharge rate, pure PCM BTMS achieved a higher average Nusselt number, as the PCM did not undergo phase change. Additionally, when comparing the average Nusselt numbers for different PCM based BTMS configurations (pure PCM, PCM with solid fins, and PCM with porous fins) under various discharge rates, the average Nusselt number was higher for lower discharge rates. This is due to longer discharge times at lower discharge rates, allowing the BTMS more time to extract the generated heat until the end of discharge.

Further enhancement of the BTMS was investigated by introducing liquid cooling to the PCM with porous fin BTMS. As shown in Fig. 6, compared to the pure PCM BTMS, the PCM with porous fins and liquid cooling BTMS reduced $T_{Max,Sur}$ by 8.89 K, 6.14 K, and 6.10 K for 5C, 3C, and 1C discharge rates, respectively. By adding a porous layer to the liquid cooling section, the PCM with porous fins and liquid cooling HBTMS further reduced $T_{Max,\ Sur}$ by 9.18 K, 6.75 K, and 6.33 K for 5C, 3C, and 1C discharge rates, respectively. For the 1C discharge rate, due to less heat generation, $T_{Max,\ Sur}$ even fell below the ambient temperature of 308.15 K. The generated heat, conducted to the cooling plates through the battery housing, PCM, porous fins, PCM housing, and cooling plates, was dissipated by forced convection due to the water flow in the copper tube. The presence of the porous layer also enhances the forced convection within the copper tube.

As illustrated in Fig. 10(a), the introduction of a porous layer significantly modifies the parabolic velocity profile at the middle of the copper tube along the vertical axis. The porous layer introduces resistance, resulting in a reduced velocity in this region, falling below the

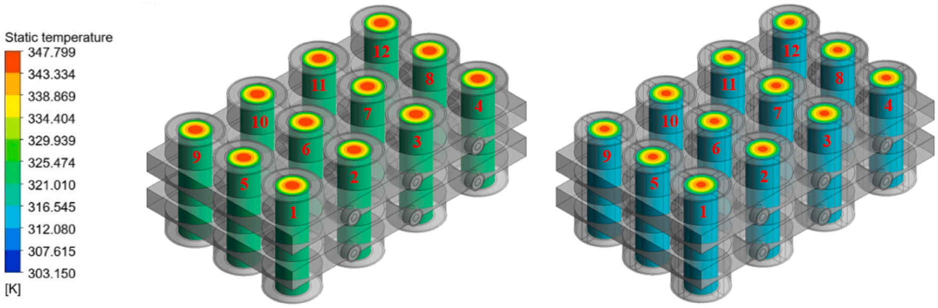

(a) Pure PCM

(b) PCM with solid fins

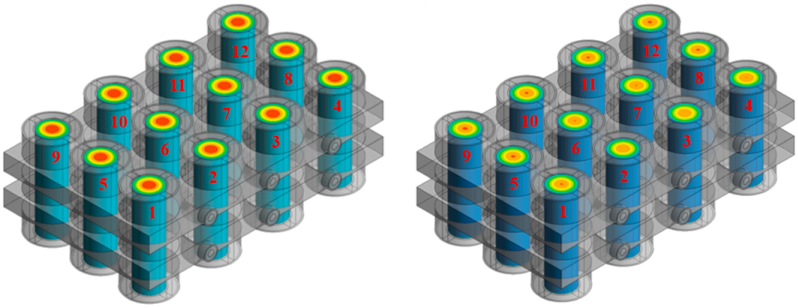

(c) PCM with porous fins

(d) PCM with porous fins and liquid cooling

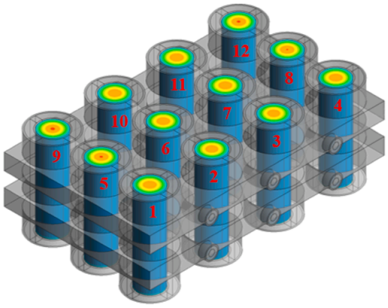

(e) PCM with porous fins and liquid cooling with porous layer

Fig. 12. Static temperature contour plots for different BTMSs and HBTMS at the end of the 5C discharge rate.

mean velocity. This resistance also creates a steeper velocity gradient near the interface between the porous medium and the clear fluid region. Consequently, mixing is enhanced near the copper tube wall, where the porous layer provides higher thermal conductivity. In the open, more permeable region at the core of the copper tube, the fluid velocity is approximately 1.75 times higher compared to the tube without a porous layer.

The dimensionless temperature profile within the copper tube is defined as follows [77]:

$$\theta = \frac{k_{s_{eff}}\left(T - T_{w,tube}\right)}{q_{w,\mathrm{tube}}D} \tag{43}$$

where $T_{w,tube}$ and $q_{w,\mathrm{tube}}$ are the copper tube wall temperature and heat flux, respectively. D is the diameter of the copper tube.

The temperature profile shown in Fig. 10(b) reveals the impact of the porous layer on temperature distribution. The continuous profile observed in the copper tube without porous layer was altered, displaying a disconnection in temperature distribution upon the insertion of the porous layer. The higher temperature of the liquid phase within the porous layer, compared to the temperature in the absence of a porous layer, indicates enhanced heat removal from the surface of the copper tube. This enhancement is attributed to the increased heat transfer surface area provided by the copper foam's ligaments. Additionally, a considerable temperature difference between the solid and liquid phases within the porous layer is evident. This disparity arises from the significantly higher thermal conductivity of the copper foam compared to the water flowing through the porous layer. Furthermore, the ligaments within the porous medium disrupt the formation of the thermal boundary layer.

Introducing liquid cooling to the system significantly impacts the PCM melting process, causing a noticeable delay in the melting onset of the PCM. As presented in Fig. 7, the L_f value dramatically decreased for different HBTMS configurations with liquid cooling. Compared to pure PCM BTMS, for the 5C discharge rate, a reduction of 86 % and 94 % was observed for BTMS with liquid cooling and HBTMS with liquid cooling and a porous layer, respectively. For lower discharge rates, introducing liquid cooling prevented the PCM from melting during discharge. Moreover, comparing PCM liquid fraction contour plots in Fig. 8(a), (d), and (e), under the 5C discharge, it can be seen that with liquid cooling, PCM mostly melted within the porous fins and around the battery housing, while PCM near the PCM housing remained solid due to enhanced heat transfer by cooling plates. For batteries 1 to 4, which are close to the liquid cooling inlet, less PCM melted. However, as water absorbed heat along the copper tube, causing an inlet temperature rise, the portion of melted PCM increased, especially for batteries 9 to 12. Additionally, for batteries 2, 3, 6, 7, 10, and 11, which are surrounded by copper tubes in the cooling plates, a smaller proportion of the PCM melted. In contrast, for batteries on the side of the pack were less affected by liquid cooling, more heat was absorbed as latent heat by

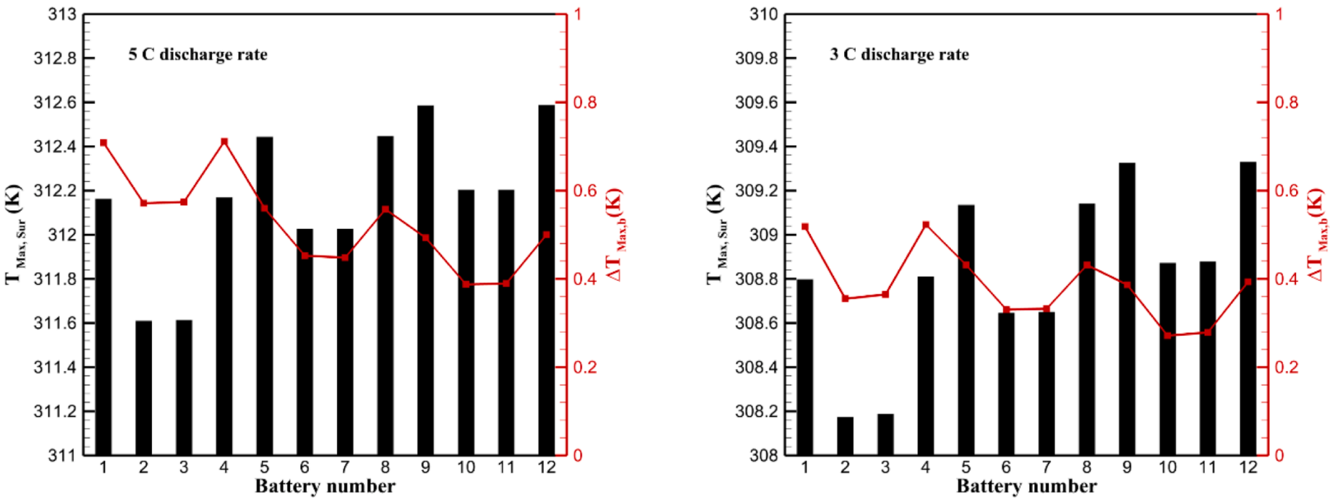

(a) 5C

(b) 3C

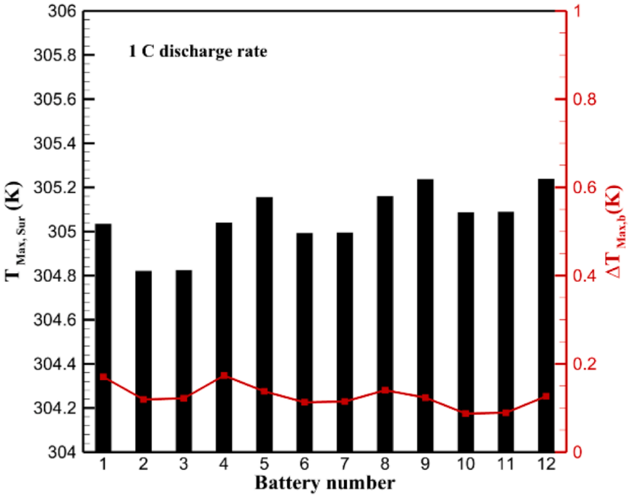

(c) 1C

Fig. 13. $T_{Max,\ Sur}$, ΔT_{Max}, at the end of discharge for the HBTMS under investigation for different discharge rates.

PCM.

As illustrated in Fig. 9(a), under a 5C discharge rate, at the end of discharge, the HBTMS with liquid cooling and a porous layer, as well as the HBTMS with liquid cooling alone, increased the average Nusselt number by approximately 13 times and 9 times, respectively, compared to the pure PCM BTMS. Fig. 9(b) shows that under a 3C discharge rate, the improvement is approximately twofold and threefold, respectively. Therefore, it can be concluded that HBTMS with liquid cooling is particularly suitable for high discharge rates.

Effective BTMS design needs to consider not only reducing the maximum temperature but also minimizing the maximum temperature difference to maintain a uniform temperature distribution within the battery pack and individual battery cells. Thus, the maximum temperature difference with the battery pack (ΔT_{Max}) has been considered as the second evaluation criterion. According to the literature, ΔT_{Max} should be kept below 5 K [9,12,13]. As shown in Fig. 11, ΔT_{Max} increased for higher discharge rates in improved HBTMS compared to pure PCM BTMS. Based on the melting start time in Fig. 7 for different discharge rates and various BTMSs, it was concluded that in BTMSs having the PCM melted, a reduction in ΔT_{Max} was observed after the onset of melting, especially at higher discharge rates. For lower discharge rates, a uniform and slight change in ΔT_{Max} was noted for different BTMSs. Additionally, more fluctuations were recorded for HBTMS with liquid cooling and liquid cooling with a porous layer, but in all cases, ΔT_{Max} remained well below 5 K. The acceptable ΔT_{Max} provided by different BTMSs is attributed to the innovative design of the housing around the battery cells, which connects to the cooling plates and prevents direct PCM contact with the battery. Moreover, as shown in contour plots in Fig. 12, this housing ensures a uniform temperature distribution on the battery surface. The temperature gradient observed in the radial direction of the batteries is due to the lower thermal conductivity in this direction compared to the axial direction.

To closely evaluate the performance of the proposed HBTMS, the battery maximum surface temperature difference ($\Delta T_{Max,b}$) and $T_{Max,Sur}$ at the end of discharge for each battery cell under various discharge rates are presented in Fig. 13. As shown, under different discharge rates,

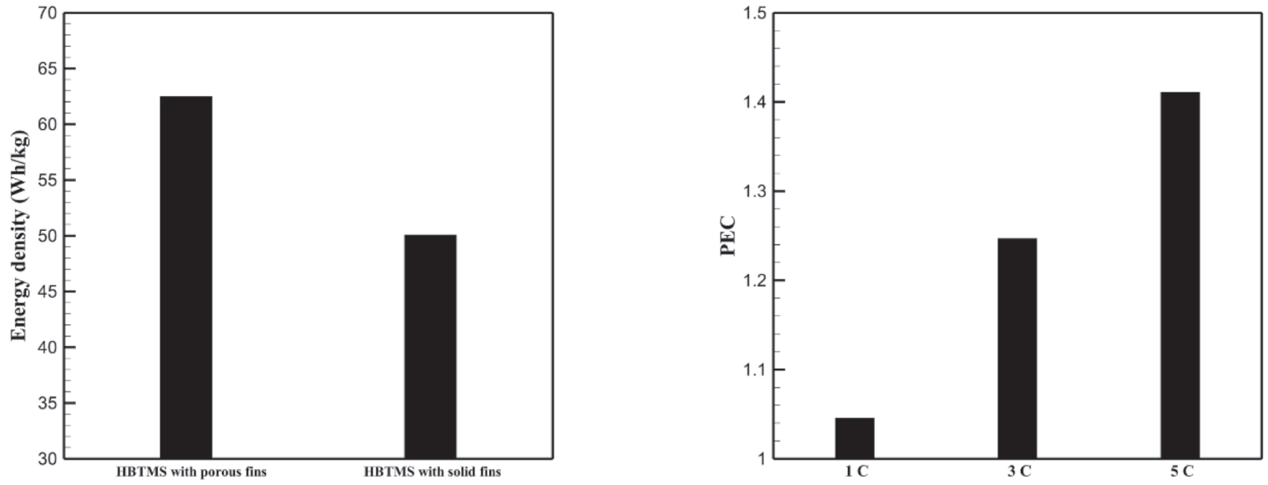

(a)

(b)

Fig. 14. Comparison of HBTMS performance in terms of (a) energy density with different fin configurations and (b) PEC value at various discharge rates..

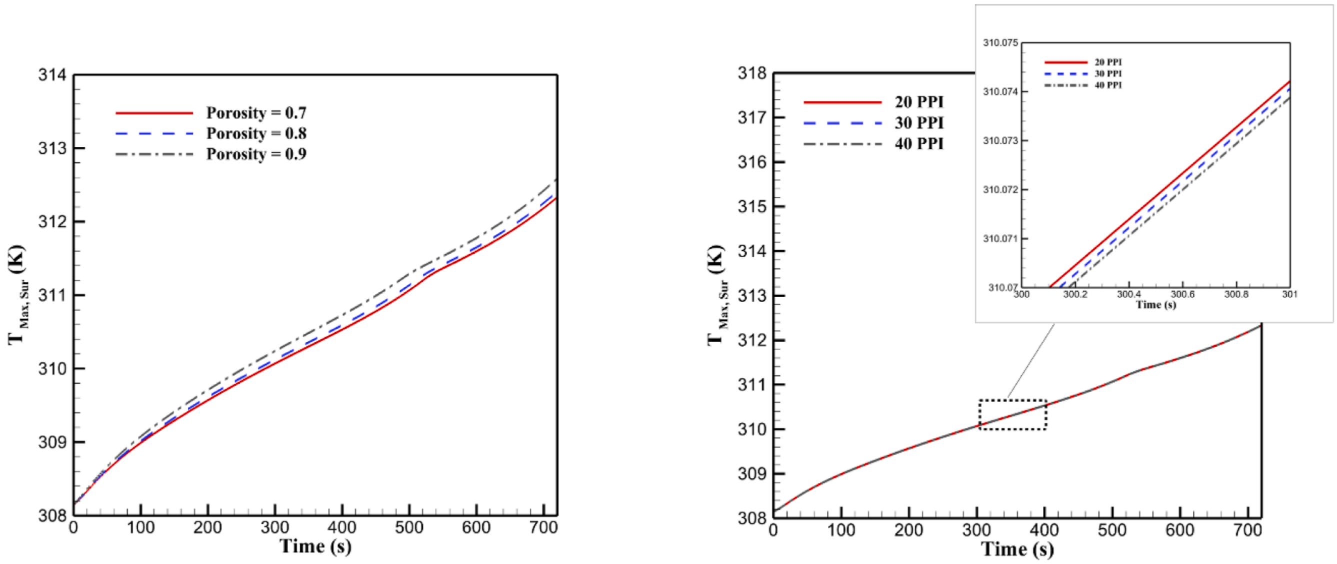

(a)

(b)

Fig. 15. Effect of porous fin properties on maximum battery surface temperature in terms of (a) porosity and (b) pore density.

the battery cells located on the sides of the battery pack (1, 4, 5, 8, 9, 12) exhibited higher $T_{Max,Sur}$ compared to those in the middle (2, 3, 6, 7, 10, 11). Fig. 12(e) demonstrates that the static temperature of the batteries was lower for battery cells near the inlet and middle of the pack, while the highest temperature at the battery cores was found on the sides and in the last row of the pack. The middle battery cells benefit more from the liquid cooling with a porous layer due to their vicinity to the copper tubes in the cooling plates. Additionally, as water flows through the copper tube, the liquid cooling's heat removal capacity decreases, leading to an increase in the inlet temperature. Consequently, for all discharge rates, the maximum and minimum $T_{Max,Sur}$ values are observed in batteries 12 and 2, respectively. In terms of $\Delta T_{Max,b}$, the HBTMS maintains it below 1 K even at a high discharge rate of 5C. As the discharge rate decreases, a more uniform temperature distribution is achieved due to the reduced heat generation rate.

Considering the impact of fin type on HBTMS's energy density based on the equation (44) [78], Fig. 14(a) shows that due to their porous structure, porous fins weigh less than solid fins. Consequently, the energy density for HBTMS with porous fins is approximately 25 % higher compared to HBTMS with solid fins. Therefore, porous fins outperform solid fins in terms of energy density.

$$E_d = \frac{UC_0}{m} \tag{44}$$

where E_d represents the energy density, U denotes the battery's nominal voltage, C_0 indicates the battery's nominal capacity, and m signifies the

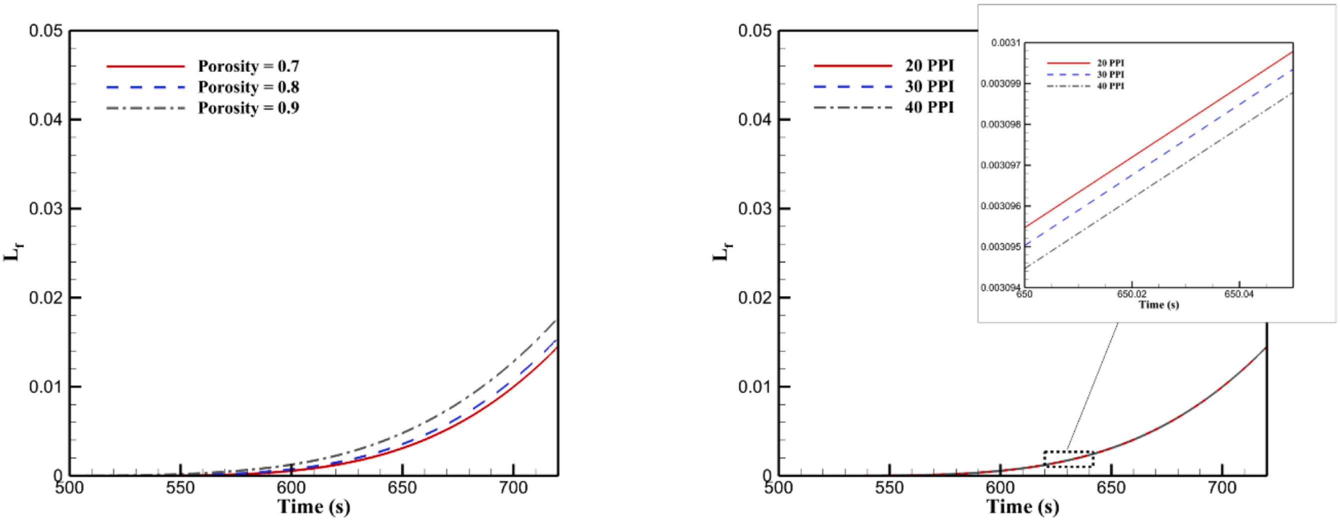

(a) (b)

Fig. 16. Effect of porous fin properties on PCM liquid fraction in terms of (a) porosity and (b) pore density.

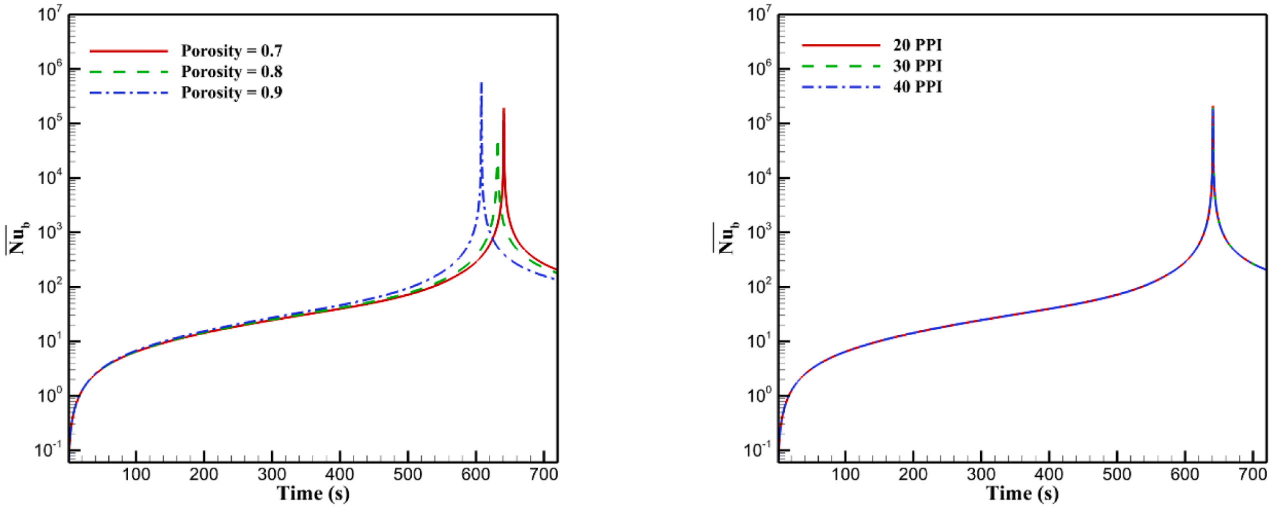

(a) (b)

Fig. 17. Effect of porous fin properties on the average Nusselt number on the battery surface in terms of (a) porosity and (b) pore density.

mass of the BTMS.

Inserting porous layers within the copper tube increases the heat transfer rate but also results in a higher pressure drop. Therefore, balancing these parameters is crucial. To evaluate the heat transfer performance, based on Eq. (45), the performance evaluation criteria (PEC) [79] was utilized. The PEC value provides a comparison of the Nusselt number and pressure drop for the liquid cooling with and without porous layer in the copper tube, while maintaining all other geometric characteristics of the HBTMS constant. As shown in Fig. 14 (b), for various discharge rates, PEC values exceed one, indicating that the increase in heat transfer rate due to the porous layer outweighs the rise in pressure drop. The enhanced HBTMS performance is more pronounced at higher discharge rates.

$$PEC = \frac{\overline{Nu}/\overline{Nu}_0}{\left(\overline{f}_r/\overline{f}_{r0}\right)^{1/3}} \tag{45}$$

where $\overline{Nu}$ and $\overline{f}_r$ are the average Nusselt number for liquid cooling and friction factor, respectively, are defined as follows:

$$\overline{Nu} = \frac{\overline{h}D}{K_f} \tag{46}$$

where $\overline{h}$, D, and K_f represent the average convection heat transfer coefficient, copper tube inner diameter, and water thermal conductivity, respectively.

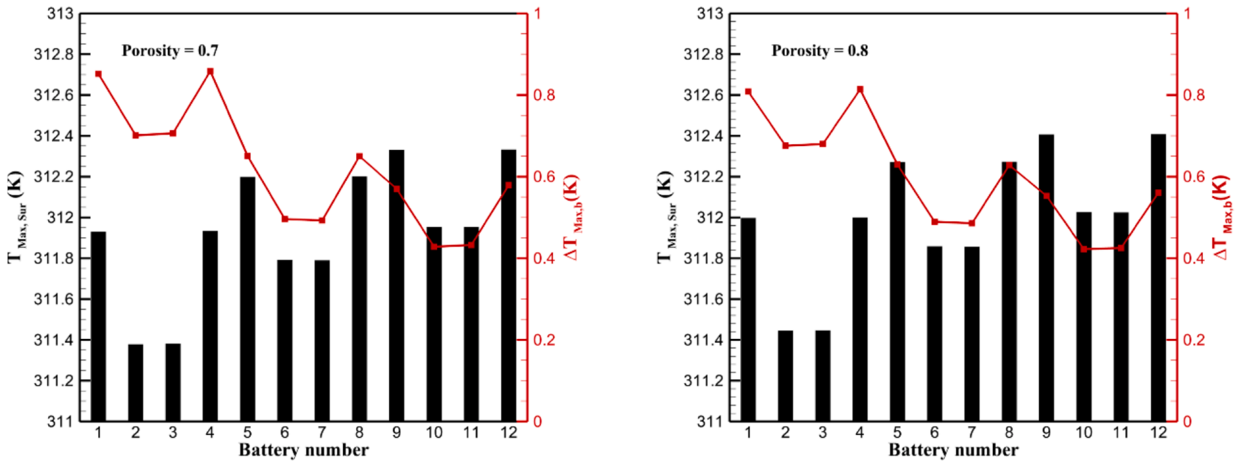

Porosity = 0.7

Porosity = 0.8

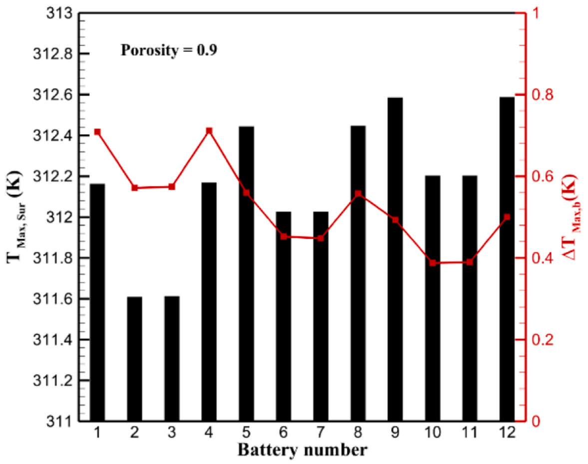

Porosity = 0.9
(a)

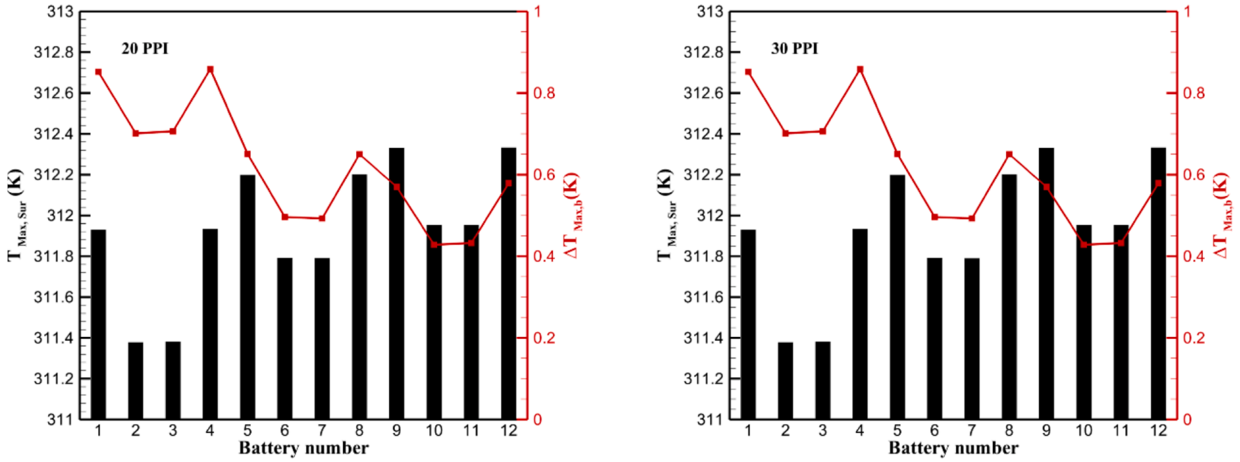

20 PPI

30 PPI

Fig. 18. $T_{Max,\ Sur}$, $\Delta T_{Max,b}$ at the end of discharge for the HBTMS with different porous fins' (a) porosity and (b) pore density.

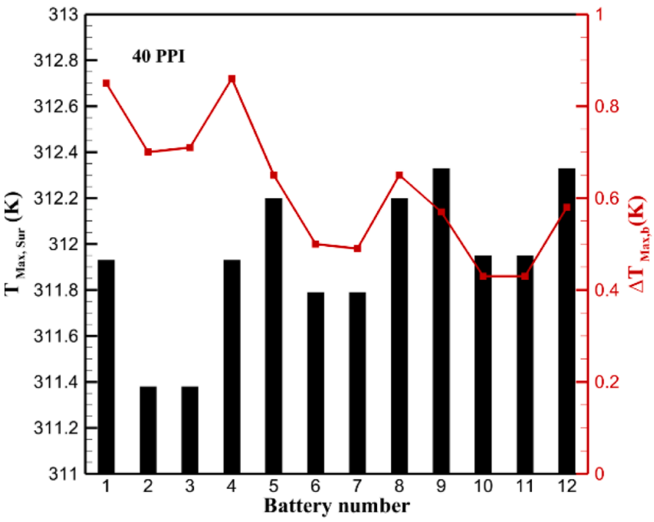

40 PPI
(b)

Fig. 18. (*continued*).

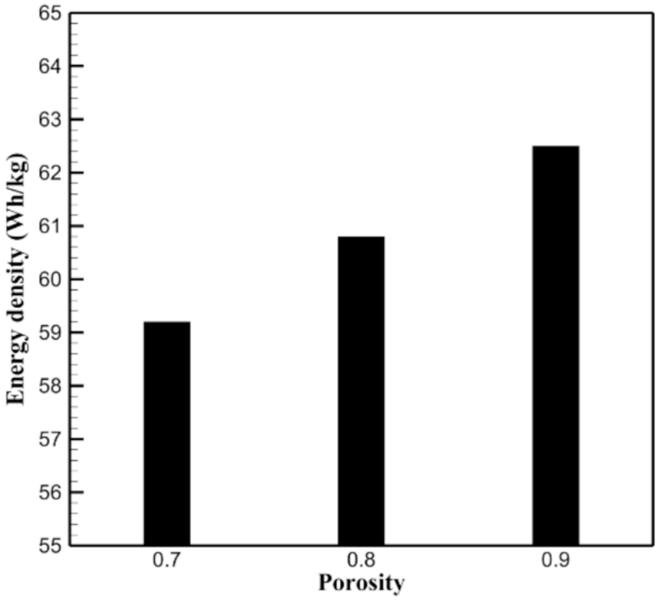

Fig. 19. Comparison of energy density for HBTMS with different porous fins' porosity.

$$\overline{f_r} = \frac{\Delta P}{\rho_f U_{inlet}^2} \tag{47}$$

where ΔP, ρ_f, and U_{inlet} denote the pressure drop along the copper tube, water density, and inlet velocity, respectively.

4.2. *Impact of porous fins porosity and pore density*

Porosity and pore density are critical characteristics of porous media that significantly influence their permeability and thermal performance. In this section the effects of porosity (0.7, 0.8, and 0.9) and pore density (20, 30, and 40 PPI) of porous fins on the performance and design features of the HBTMS system have been investigated. The porosity and pore density of the porous layers within the copper tube have been considered constant at 0.9 and 30 PPI, respectively.

As previously demonstrated, the inclusion of porous fins significantly impacts PCM performance by enhancing its thermal conductivity. Fig. 15 and Fig. 16 illustrate that porosity has a greater effect on $T_{Max, Sur}$, and L_f compared to pore density. Fig. 15(a) shows that $T_{Max, Sur}$ decreases by considering porous fins with lower porosity. At the end of discharge, compared to a high porosity of 0.9, $T_{Max, Sur}$ decreases by 0.18 K and 0.25 K for porosities of 0.8 and 0.7, respectively. Fins with reduced porosity have more solid material (copper) and smaller voids, which generally provide better thermal conductivity due to increased conduction paths within the PCM. However, as shown in Fig. 16(a), higher porosities, which result in fins with larger voids and more PCM within the pores, lead to higher L_f values. For porosities of 0.9 and 0.8, the L_f value is approximately 22 % and 7 % higher than that of a porosity of 0.7 at the end of discharge, respectively. Additionally, PCM melting onset occurs earlier for lower porosities; for instance, melting begins at 495 s for a porosity of 0.7 under a 5C discharge rate, which is 22 s and 31 s earlier than for porosities of 0.8 and 0.9, respectively.

Regarding the impact of pore density, Fig. 15(b) and Fig. 16(b) depict that $T_{Max, Sur}$, and L_f are not significantly influenced by pore density. Since porosity was kept constant, the amount of metal used remains unchanged. Comparing 20 PPI to 40 PPI, the system contains fewer pores per unit length at 20 PPI. To maintain constant porosity, the area of the metal between pores must be greater for 20 PPI compared to 40 PPI, resulting in higher heat conductivity. Conversely, at 40 PPI, the PCM was divided by a larger number of encapsulations, enhancing performance compared to 20 PPI. Therefore, the opposing effects of increased metal area and greater encapsulation lead to a negligible overall impact on temperature and liquid fraction. Additionally, with constant porosity, the volume fraction of PCM remains the same across different PPI values.

As depicted in Fig. 17, the average Nusselt number on the battery surface is more significantly affected by porosity than by pore density. Specifically, Fig. 17(a) demonstrates that after the onset of PCM melting, porous fins with lower porosity lead to a higher average Nusselt number. This is due to the fact that lower porosity enhances both heat conduction and effective convection at the pore scale, thereby improving overall heat transfer. At the end of discharge, compared to a porosity of 0.9, the average Nusselt number was improved by 33 % and 52 % for porosities of 0.8 and 0.7, respectively. Conversely, Fig. 17(b) indicates that with constant porosity, variations in pore density do not affect the average Nusselt number, as changes in pore density have a minimal impact on

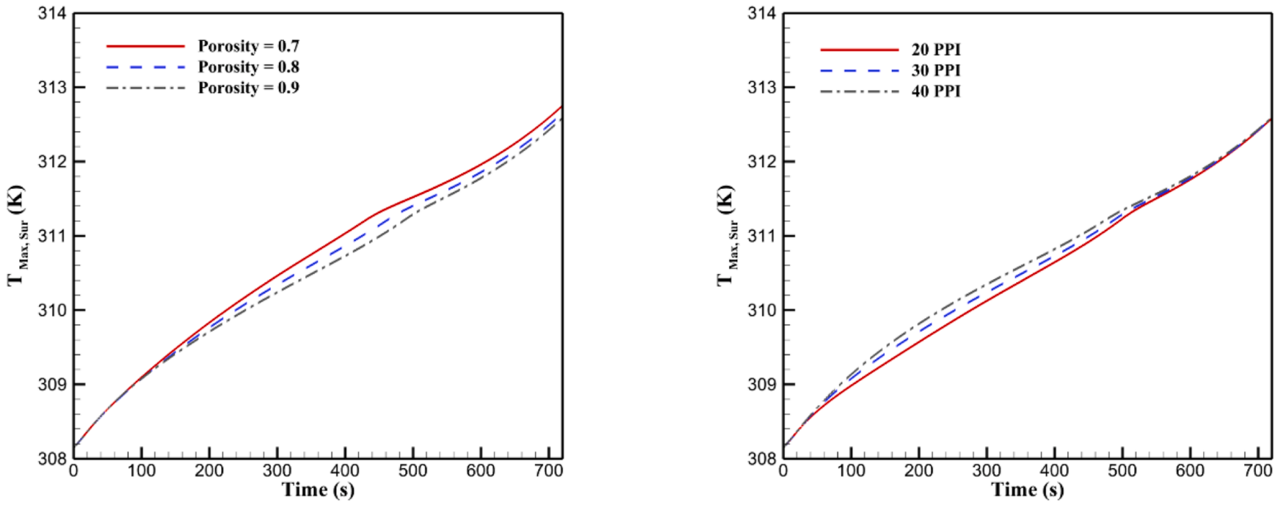

(a)

(b)

Fig. 20. Effect of porous layer properties on maximum battery surface temperature in terms of (a) porosity and (b) pore density.

PCM melting and battery surface temperature.

Considering the state of individual battery cell within the battery pack at the end of a 5C discharge, as shown in Fig. 18, a similar trend in $T_{Max,\ Sur}$, and $\Delta T_{Max,b}$ was observed for different porosities of the porous fins, with lower values for the lower porosity of 0.7. Battery cells close to the inlet section and in the middle of the battery pack tend to have lower $T_{Max,\ Sur}$. Moreover, higher $\Delta T_{Max,b}$ was found to occur in battery cells on the side of the pack, including batteries 1, 4, 5, 8, 9, and 12, as these battery cells were less affected by liquid cooling. As depicted in Fig. 18, almost similar $T_{Max,\ Sur}$, and $\Delta T_{Max,b}$ was recorded for various pore density of the porous fins, indicating that pore density has minimal impact on these parameters.

As depicted in Fig. 19, the energy density of the system was significantly affected by the porous fins' porosity. Lower porosities contain more copper, which has a higher density, thereby increasing the system's weight and negatively impacting the energy density. Consequently, when considering porous fins with higher porosity compared to a porosity of 0.7, the energy density increased by approximately 3 % and 6 % for porosities of 0.8 and 0.9, respectively.

4.3. Impact of porous layers porosity and pore density within the copper tube

As demonstrated in the previous sections, HBTMS based on liquid cooling with a porous layer was found to be more effective. Therefore, this section investigates the properties of the porous layer within the copper tube, specifically in terms of porosity (0.7, 0.8, and 0.9) and pore density (20, 30, and 40 PPI), and their impact on system cooling performance. For this analysis, the porosity and pore density of the porous fins were kept constant at 0.9 and 30 PPI, respectively.

As depicted in Fig. 20(a), in contract to porous fins' porosity (Fig. 15 (a)), increasing the porous layer porosity results in lower $T_{Max,\ Sur}$. At the end of the 5C discharge, compared to a porosity of 0.7, $T_{Max,\ Sur}$ is reduced slightly by 0.1 K and 0.16 K for porosities of 0.8 and 0.9, respectively. Increased porosity leads to a higher number of voids within the porous material and as shown in Fig. 21(a) enhancing the penetration and flow of the cooling fluid through the porous layer. Also, as more liquid passes through the porous layer, the velocity of the fluid in the core of the copper tube declines, when compared to porosity of 0.7, the maximum dimensionless velocity value declines by 42 % and 50 % for porosities of 0.8 and 0.9, respectively. By more penetration of the fluid into the porous layer with higher porosity, the mixing of the fluid increases in the vicinity of the copper tube surface. Comparing the dimensionless temperature profile for solid phase for different porosities in Fig. 21(b) depicts higher temperature for lower porosity of 0.7 due to improved effective thermal conductivity. However, dimensionless temperature of the liquid phase within the porous layer was observed to be higher for the porosity of 0.9 which depicts better heat removal from the copper tube surface.

Local Nusselt number in the porous layer is defined as follows [80]:

$$Nu = -\frac{D}{(T_{Solidphase} - T_{bulk})}\frac{\partial T}{\partial y}\bigg|_{w} \tag{48}$$

The mentioned enhanced heat transfer is evident on local Nusselt number due to improved convection along the porous layer as depicted in Fig. 21(c), where the local Nusselt number increased by 24 % and 73 % for porosity of 0.8 and 0.9 respectively, compared to porosity of 0.7. This improves the transfer of generated heat from the battery to the cooling fluid, thereby reducing the $T_{Max,\ Sur}$. The impact of variations in pore density of the porous layers on $T_{Max,\ Sur}$ is shown in Fig. 20(b). In contrast to porosity, higher pore density results in higher $T_{Max,\ Sur}$. During the discharge, the maximum difference in $T_{Max,\ Sur}$ for 30 PPI and 40 PPI compared to 20 PPI was 0.14 K and 0.25 K, respectively. However, this difference was evident before the start of PCM melting. After approximately 500 s, porous layers with different pore densities provided almost similar $T_{Max,\ Sur}$. The physical reason for this trend is that higher pore densities at constant porosity result in smaller pore sizes, which can restrict the flow of the cooling fluid through the porous layer and as shown in Fig. 22(a) the dimensionless velocity is lower in porous layer with 40 PPI pore density compared to 20 PPI. Also, similar to porosity, the dimensionless velocity in clear region at the core of the copper tube tends to increase by increasing the pore density. As depicted in Fig. 22(b), this restriction reduces the efficiency of heat transfer from the battery to the cooling fluid, leading to higher surface temperatures. Although higher pore density provides more surface area, the limited fluid flow reduces the overall convective heat transfer effectiveness. It was also observed that according to Fig. 22(b), pore density variation seems to have less impact on local temperature distribution especially in the clear region of the copper tube. The porous layer with a 20 PPI pore

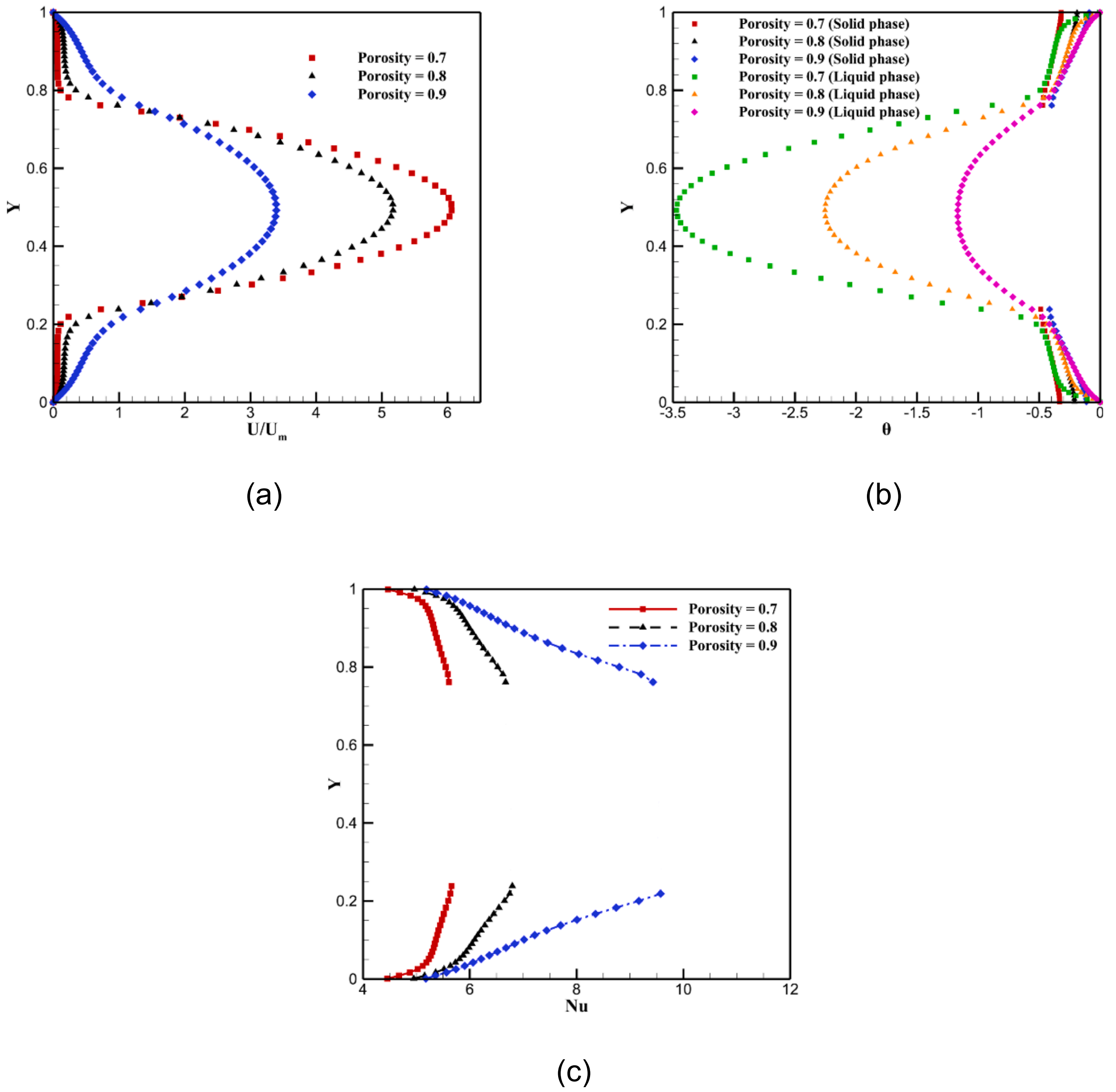

Fig. 21. Effect of porous layer porosity on (a) dimensionless velocity, (b) dimensionless temperature, and (c) local Nusselt number at the middle of the copper tube along the vertical axis at the end of 5C discharge rate.

density achieved a higher heat transfer rate due to the increased fluid flow rate in the foam region. However, its heat transfer area is smaller due to lower pore density compared to the porous layer with a 40 PPI pore density. These two opposing factors lead to only a minor difference in the local temperature. As illustrated in Fig. 22(c), variations in pore density have a minor impact on the local Nusselt number along the porous layer. While increasing the pore density with constant porosity results in similar heat conduction, it reduces convection heat transfer due to decreased permeability. Consequently, the local Nusselt number decreases with higher pore density.

As shown in Fig. 23, variations in the porosity of porous layers have a greater impact on L_f compared to changes in pore density. When the heat transfer enhancement capability of the porous layers is reduced, more heat is absorbed by the PCM, resulting in more extensive PCM melting. Fig. 23(a) indicates that the onset of PCM melting is affected by porosity; compared to a porosity of 0.7, delays of 58 s and 34 s were recorded for porosities of 0.8 and 0.9, respectively. The opposite trend was observed for various pore densities, with increased pore density causing PCM to start melting earlier.

The impact of the porous layers' porosity and pore density on the average Nusselt number on the battery surface is depicted in Fig. 24. As shown, due to the improved heat transfer rate associated with higher porosities, the Nusselt number is higher for the porosity of 0.9 compared to lower porosities, particularly after the onset of PCM melting. At the end of the discharge, the Nusselt number is approximately 31 % and 16 % higher for porosities of 0.9 and 0.8, respectively, compared to a

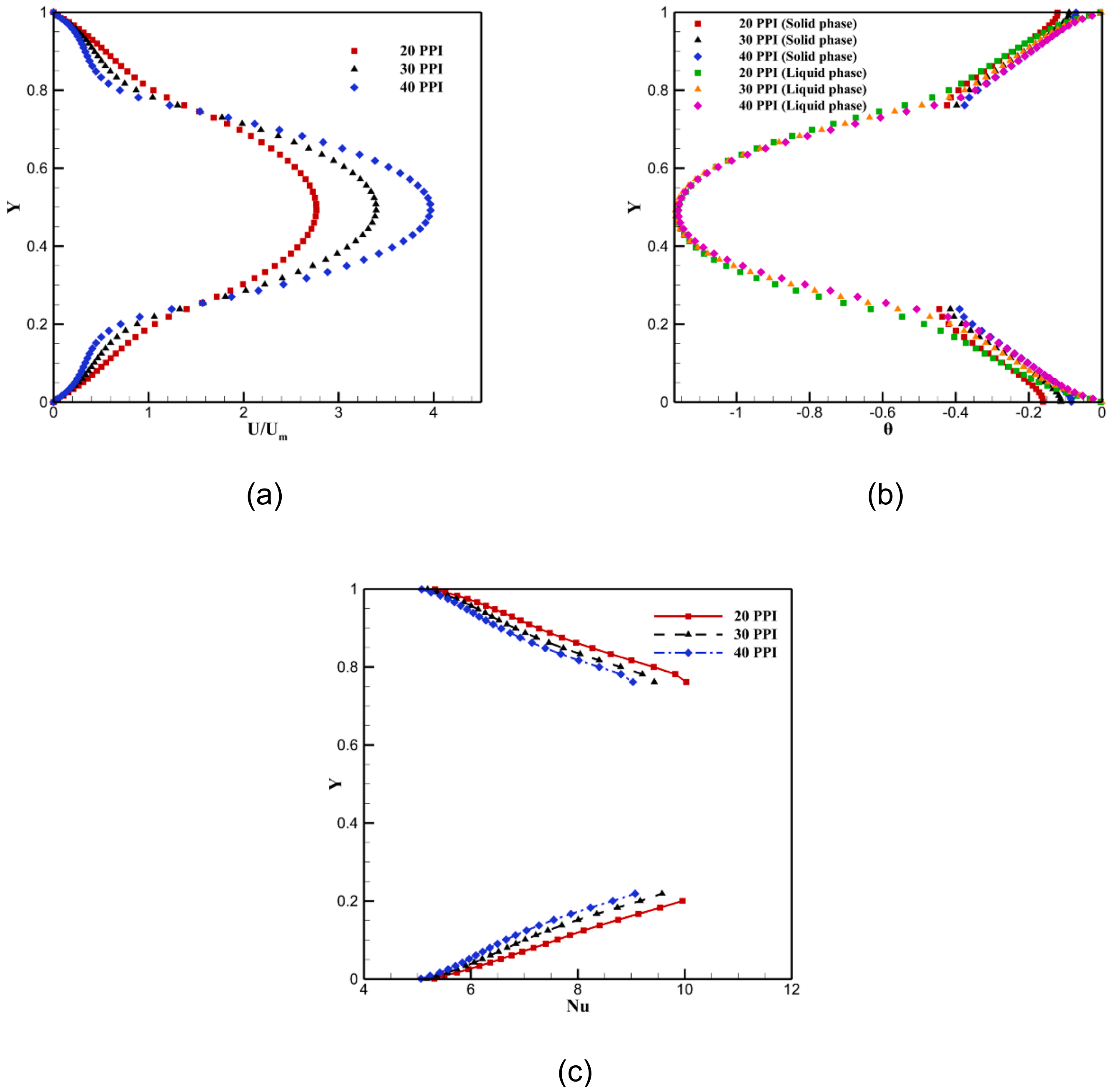

Fig. 22. Effect of porous layer pore density on (a) dimensionless velocity, (b) dimensionless temperature, and (c) local Nusselt number at the middle of the copper tube along the vertical axis at the end of 5C discharge rate.

porosity of 0.7. In contrast, the Nusselt number is less affected by pore density and tends to decrease with increasing pore density. At the end of discharge, the Nusselt number is reduced by about 1 % and 3 % for pore densities of 30 PPI and 40 PPI, respectively, compared to 20 PPI.

Fig. 25 provides the $T_{Max,\ Sur}$ and $\Delta T_{Max,\ b}$ of different battery cells at the end of the 5C discharge. Similar to previous cases, the batteries in the middle of the pack, which are surrounded by liquid cooling, experience lower $T_{Max,\ Sur}$, while batteries 9 and 12 in the last row have the highest $T_{Max,\ Sur}$. In terms of $\Delta T_{Max,\ b}$, the battery cells on the sides of the pack exhibit a higher maximum surface temperature difference. A similar pattern was observed for different porosities and pore densities. This indicates that the position within the pack and the surrounding cooling conditions significantly influence the thermal behavior of the batteries, regardless of the porosity or pore density of the porous layers.

To compare the increasing pressure drop and improved heat transfer offered by porous layers within the copper tube, the PEC value is depicted for different porosities and pore densities in Fig. 26. For a lower porosity of 0.7, the increasing pressure drop outweighs the higher heat transfer rate, resulting in a PEC value below one, indicating that using porous layers with low porosity is not advisable. However, for higher porosities of 0.8 and 0.9, the PEC value improves by 53 % and 114 %, respectively, compared to a low porosity of 0.7. These higher porosities yield PEC values above one. For a constant porous layer porosity of 0.9, as shown in Fig. 26(b), the highest PEC value is achieved with a pore density of 30 PPI, which is about 12 % and 8 % higher compared to pore densities of 20 PPI and 40 PPI, respectively. This indicates that a balance between pore density and porosity of the porous layer can optimize both pressure drop and heat transfer performance.

As demonstrated in Fig. 27, the energy density of the systems is proportionally related to the porosity of the porous layers. Compared to

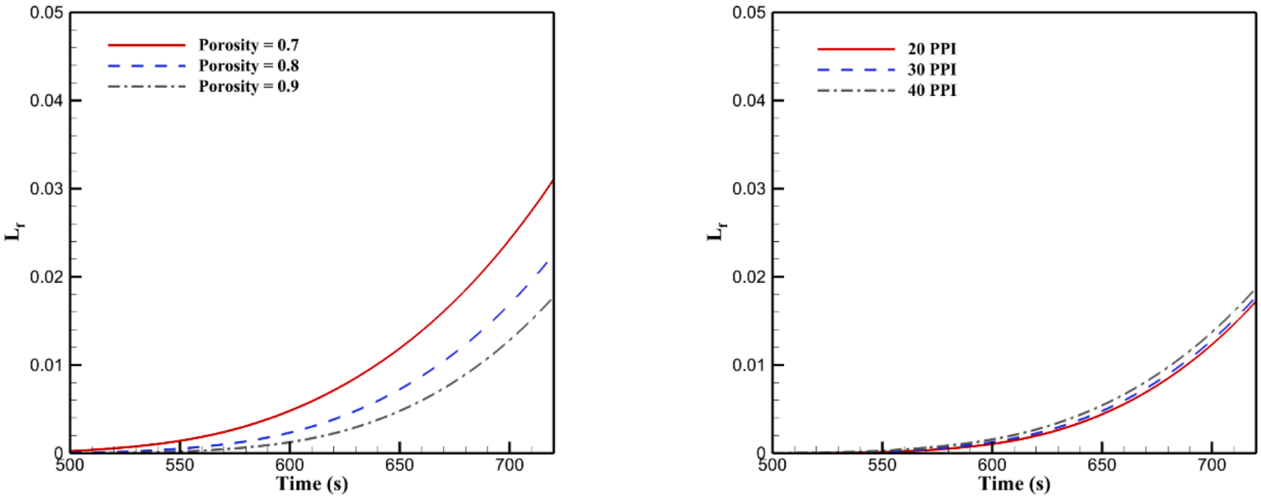

(a)

(b)

Fig. 23. Effect of porous layer properties on PCM liquid fraction in terms of (a) porosity and (b) pore density.

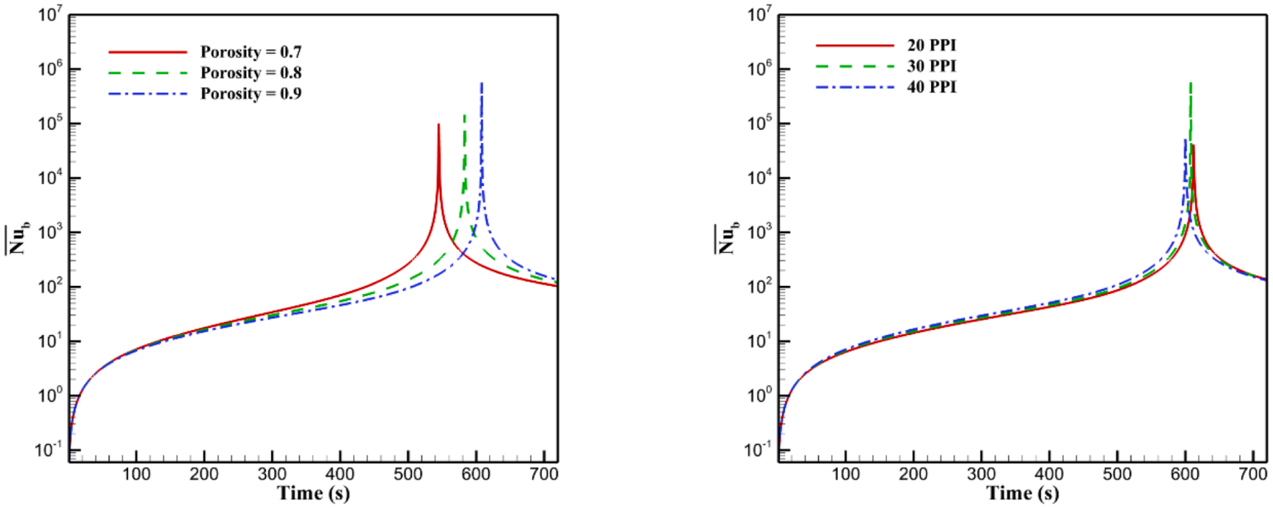

(a)

(b)

Fig. 24. Effect of porous layer properties on the average Nusselt number on the battery surface in terms of (a) porosity and (b) pore density.

a porosity of 0.7, increasing the porosity to 0.8 and 0.9 results in 1.3 % and 2.8 % improvements in energy density, respectively. This enhancement is due to the fact that higher porosity typically means more void space within the material, leading to a reduction in the overall weight of the system. A reduction in weight without compromising energy capacity results in an increase in energy density.

In practical applications, the minimal impact of pore density on thermal performance suggests that the selection of metal foams with varying pore density and constant porosity is more influenced by factors such as mechanical strength, manufacturability, and cost, rather than thermal performance [81]. While porous fins with lower porosities typically provide better heat transfer due to improved thermal conductivity, higher porosity porous fins are often favoured for their ability to increase energy density, which is essential for efficient system design. The slight reduction in thermal performance associated with higher porosity porous fins is offset by the benefits of reduced system weight and enhanced energy efficiency. A porous layer with higher porosity also improves cooling fluid flow and heat transfer, while increased pore density, despite offering more surface area, can restrict fluid flow and slightly reduce heat transfer efficiency. Therefore, balancing porosity and pore density in the porous layer is key to optimizing system performance. According to the obtained results, higher porosities are recommended for their superior energy density and improved cooling effectiveness, making them ideal for applications prioritizing efficiency and performance.

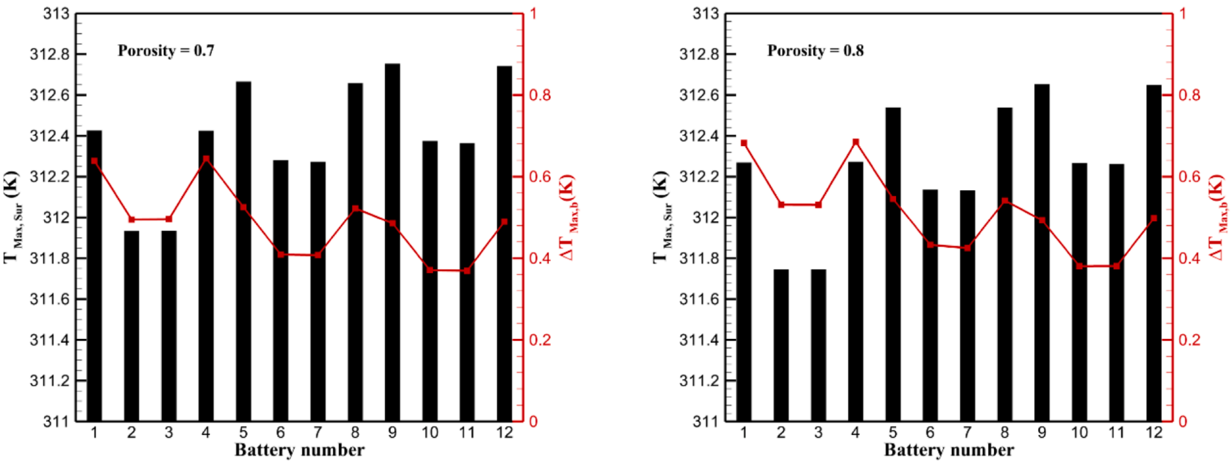

Porosity = 0.7 Porosity = 0.8

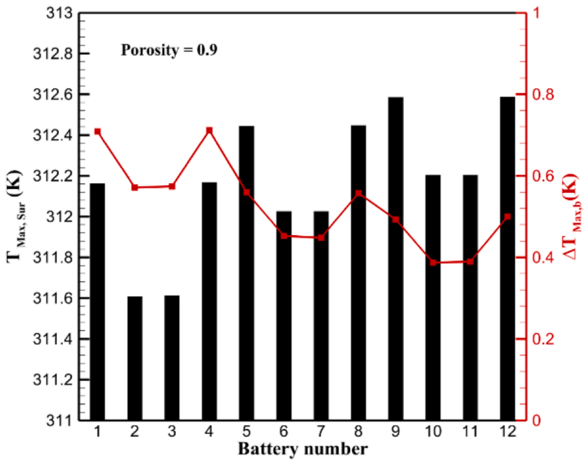

Porosity = 0.9

(a)

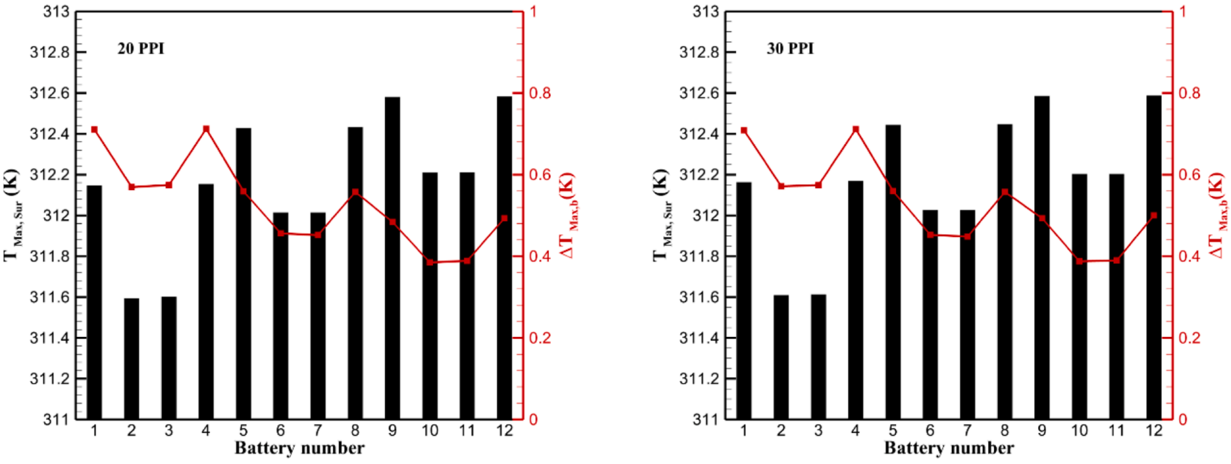

20 PPI 30 PPI

Fig. 25. $T_{Max,\ Sur}$, $\Delta T_{Max,b}$ at the end of 5C discharge for the HBTMS with different porous layers' (a) porosity and (b) pore density.

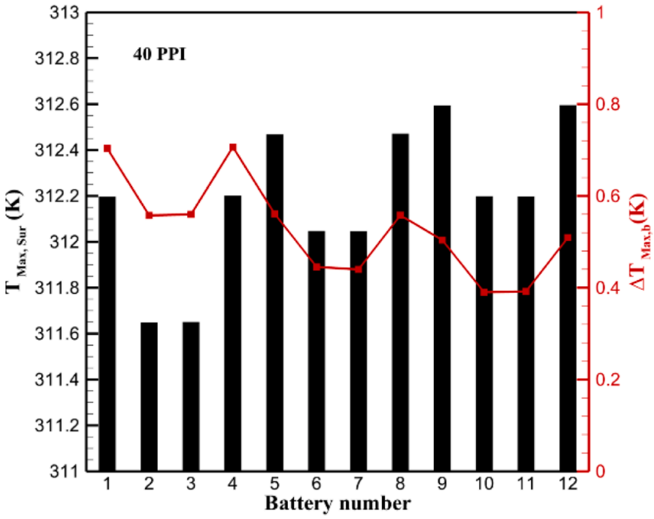

40 PPI
(b)

Fig. 25. (*continued*).

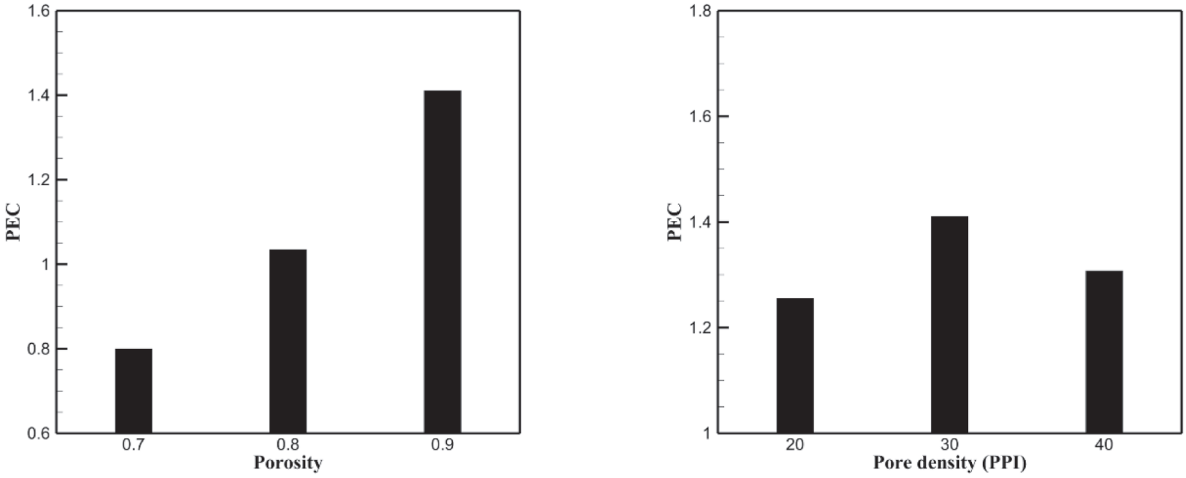

(a) (b)

Fig. 26. Effect of porous layer properties on PEC in terms of (a) porosity and (b) pore density.

5. Conclusion

The implementation of a battery thermal management system is essential for enhancing the efficiency, safety, and durability of lithium-ion batteries (LIBs). In the present numerical investigation, a hybrid battery thermal management system (HBTMS) has been studied, that integrates phase change material (PCM), copper foam as porous fins and porous layers, and liquid cooling. In contrast to earlier research efforts that primarily focus on conventional solid fins or single cooling mechanisms, this investigation aims to bridge this gap in the literature by optimising the properties of porous fins and layers in HBTMS to achieve significant improvements in both thermal performance and energy density. These enhancements are realised through improved conduction and convection, enabled by the integration of porous media within the PCM and liquid cooling plates, as well as the unique structure of the porous media with interconnected pores. Transient LIB heat generation was modelled using the Bernardi equation, incorporating resistive and entropic heat generation. The HBTMS was compared with PCM based BTMS configurations, including pure PCM, PCM with solid fins, PCM with porous fins, and PCM with porous fins combined with liquid cooling without any porous layers. The impact of the porosity (0.7, 0.8, and 0.9) and pore density (20, 30, and 40 PPI) of the copper foam as porous fins and porous layer have been analysed on HBTMS thermal and design performance. The conclusions are as follows:

- The proposed HBTMS incorporating PCM with porous fins and liquid cooling with porous layers significantly reduced the $T_{Max,Sur}$ by 9.18 K (2.9 %) compared to the pure PCM BTMS. The $T_{Max,Sur}$ reduction for PCM with solid fins, PCM with porous fins, and PCM with porous

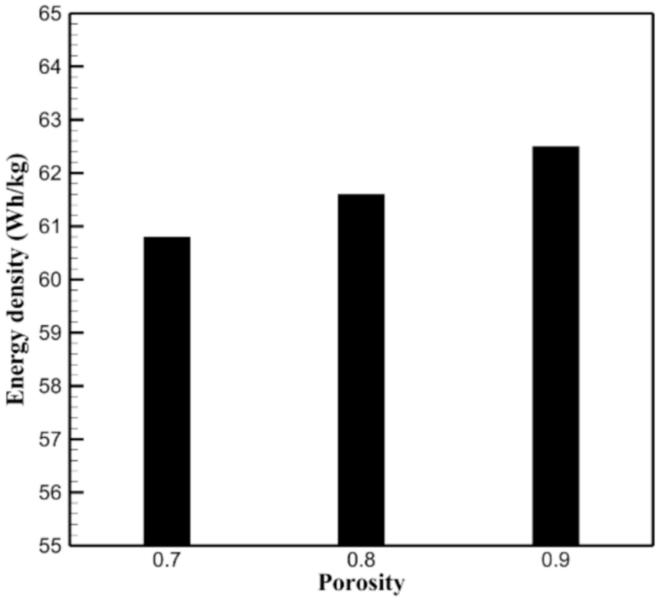

Fig. 27. Comparison of energy density for HBTMS with different porous layers' porosity.

fins and liquid cooling were 6.6 K (2.1 %), 7.52 K (2.3 %), and 8.89 K (2.8 %), respectively, compared to pure PCM BTMS.

- Compared to pure PCM BTMS at a 5C discharge rate, the L_f was reduced by 86 % and 94 % by HBTMS with liquid cooling and a porous layer, respectively. The onset of PCM melting was significantly delayed in the proposed HBTMS, ensuring the PCM remains solid for a longer duration during battery discharge compared to the pure PCM BTMS.
- ΔT_{Max} was maintained well below 5 K for various HBTMS configurations, ensuring a uniform temperature distribution across the battery pack and each battery cell.
- The addition of porous layers in HBTMS provided a performance evaluation criteria (PEC) value exceeding one, indicating enhanced heat transfer outweighs the increase in pressure drop.
- The system's energy density was significantly enhanced by approximately 25 % when porous fins are used compared to solid fins. This improvement is attributed to the lower weight of the porous fins.
- Porous fins with higher porosity result in higher L_f values and a delayed onset of PCM melting, with L_f increased by approximately 22 % and 7 % and delays of 22 s and 31 s for porosities of 0.8 and 0.9, respectively, compared to a porosity of 0.7.
- Porous fins with lower porosity lead to a higher $\overline{Nu}$ on the battery surface after the onset of PCM melting, with improvements of 33 % and 52 % for porosities of 0.8 and 0.7, respectively, compared to a porosity of 0.9.
- Energy density was significantly influenced by porosity, with higher porosities of 0.8 and 0.9 resulting in increases of approximately 3 % and 6 %, respectively, compared to a porosity of 0.7.
- The $\overline{Nu}$ on the battery surface was higher for increased porosity of the porous layers within the copper tubes, showing improvements of 31 % for a porosity of 0.9 and 16 % for a porosity of 0.8, compared to a porosity of 0.7.
- The performance evaluation criteria (PEC) values were positively impacted by the increased porosity of the porous layers. For a porosity of 0.7, the PEC value was below one due to the increased pressure drop. However, higher porosities of 0.8 and 0.9 yielded PEC values above one, indicating that the enhanced heat transfer rate outweighed the increase in pressure drop.

CRediT authorship contribution statement

Alireza Keyhani-Asl: Investigation, Formal analysis, Methodology, Software, Validation, Visualization, Writing – original draft, Writing – review & editing. **Noel Perera:** Project administration, Supervision, Writing – review & editing. **Jens Lahr:** Supervision. **Reaz Hasan:** Conceptualization, Supervision, Writing – review & editing.

Funding

This research did not receive any specific grant from funding agencies in the public, commercial, or not-for-profit sectors.

Declaration of competing interest

The authors declare that they have no known competing financial interests or personal relationships that could have appeared to influence the work reported in this paper.

Acknowledgments

The authors extend their gratitude to Dr. Roger Tait for his invaluable advice and guidance in utilizing the HPC (Cluster 3) resource. Additionally, they thank the Faculty of Computing, Engineering, and the Built Environment at Birmingham City University for their support in providing access to this resource.

Data availability

Data will be made available on request.

References

[1] M. Al-Zareer, I. Dincer, M.A. Rosen, A review of novel thermal management systems for batteries, Int. J. Energy Res. 42 (10) (2018) 3182–3205.
[2] X. Zhang, Z. Li, L. Luo, Y. Fan, Z. Du, A review on thermal management of lithium-ion batteries for electric vehicles, Energy 238 (2022) 121652.
[3] J. Jaguemont, L. Boulon, Y. Dube, F. Martel, Thermal management of a hybrid electric vehicle in cold weather, IEEE Trans. Energy Convers. 31 (3) (2016) 1110–1120.
[4] Z. Lei, Z. Maotao, X. Xiaoming, G. Junkui, Thermal runaway characteristics on NCM lithium-ion batteries triggered by local heating under different heat dissipation conditions, Appl. Therm. Eng. 159 (2019) 113847.
[5] P. Ramadass, B. Haran, R. White, B.N. Popov, Capacity fade of Sony 18650 cells cycled at elevated temperatures: Part I. Cycling performance, J. Power Sources 112 (2) (2002) 606–613.
[6] F.S. Hwang, T. Confrey, C. Reidy, D. Picovici, D. Callaghan, D. Culliton, C. Nolan, Review of battery thermal management systems in electric vehicles, Renew. Sustain. Energy Rev. 192 (2024) 114171.
[7] Pesaran, A., M. Keyser, G. Kim, S. Santhanagopalan, and K. Smith, *Tools for designing thermal management of batteries in electric drive vehicles (presentation)*. 2013, National Renewable Energy Lab.(NREL), Golden, CO (United States).
[8] Z. Jiang, Z. Qu, Lithium–ion battery thermal management using heat pipe and phase change material during discharge–charge cycle: A comprehensive numerical study, Appl. Energy 242 (2019) 378–392.
[9] Z. Rao, Z. Qian, Y. Kuang, Y. Li, Thermal performance of liquid cooling based thermal management system for cylindrical lithium-ion battery module with variable contact surface, Appl. Therm. Eng. 123 (2017) 1514–1522.
[10] P. Qin, M. Liao, D. Zhang, Y. Liu, J. Sun, Q. Wang, Experimental and numerical study on a novel hybrid battery thermal management system integrated forced-air convection and phase change material, Energ. Conver. Manage. 195 (2019) 1371–1381.
[11] Z. Ling, F. Wang, X. Fang, X. Gao, Z. Zhang, A hybrid thermal management system for lithium ion batteries combining phase change materials with forced-air cooling, Appl. Energy 148 (2015) 403–409.
[12] W. Wu, S. Wang, W. Wu, K. Chen, S. Hong, Y. Lai, A critical review of battery thermal performance and liquid based battery thermal management, Energ. Conver. Manage. 182 (2019) 262–281.
[13] A. Greco, X. Jiang, D. Cao, An investigation of lithium-ion battery thermal management using paraffin/porous-graphite-matrix composite, J. Power Sources 278 (2015) 50–68.
[14] P. Zare, N. Perera, J. Lahr, R. Hasan, Solid-liquid phase change materials for the battery thermal management systems in electric vehicles and hybrid electric vehicles–A systematic review, J. Storage Mater. 52 (2022) 105026.
[15] Nield, D.A. and A. Bejan, *Convection in porous media*. Vol. 3. 2006: Springer.
[16] Vafai, K., *Handbook of porous media*. 2015: CRC Press.

[17] Mahmoudi, Y., K. Hooman, and K. Vafai, *Convective heat transfer in porous media*. 2019: CRC Press.

[18] A.K. Asl, S. Hossainpour, M. Rashidi, M.A. Sheremet, Z. Yang, Comprehensive investigation of solid and porous fins influence on natural convection in an inclined rectangular enclosure, Int. J. Heat Mass Transf. 133 (2019) 729–744.

[19] M.A. Vatanparast, S. Hossainpour, A. Keyhani-Asl, S. Forouzi, Numerical investigation of total entropy generation in a rectangular channel with staggered semi-porous fins, Int. Commun. Heat Mass Transfer 111 (2020) 104446.

[20] A. Keyhani-Asl, N. Perera, J. Lahr, R. Hasan, Porous media and foam application in battery thermal management systems: A comprehensive review focused on its impact, numerical modeling, and experimental preparation, J. Storage Mater. 93 (2024) 112306.

[21] S. Rashidi, A. Ijadi, Z. Dadashi, Potentials of porous materials for temperature control of lithium-ion batteries, J. Storage Mater. 51 (2022) 104457.

[22] H. Yang, M. Li, Z. Wang, B. Ma, A compact and lightweight hybrid liquid cooling system coupling with Z-type cold plates and PCM composite for battery thermal management, Energy 263 (2023) 126026.

[23] H.N. Khaboshan, F. Jaliliantabar, A.A. Abdullah, S. Panchal, Improving the cooling performance of cylindrical lithium-ion battery using three passive methods in a battery thermal management system, Appl. Therm. Eng. 227 (2023) 120320.

[24] Y. Zhao, B. Zou, J. Ding, Y. Ding, Experimental and numerical investigation of a hybrid battery thermal management system based on copper foam-paraffin composite phase change material and liquid cooling, Appl. Therm. Eng. 218 (2023) 119312.

[25] H. Liu, S. Ahmad, Y. Shi, J. Zhao, A parametric study of a hybrid battery thermal management system that couples PCM/copper foam composite with helical liquid channel cooling, Energy 231 (2021) 120869.

[26] M. Kiani, S. Omiddezyani, A.M. Nejad, M. Ashjaee, E. Houshfar, Novel hybrid thermal management for Li-ion batteries with nanofluid cooling in the presence of alternating magnetic field: an experimental study, Case Stud. Therm. Eng. 28 (2021) 101539.

[27] M. Kiani, M. Ansari, A.A. Arshadi, E. Houshfar, M. Ashjaee, Hybrid thermal management of lithium-ion batteries using nanofluid, metal foam, and phase change material: an integrated numerical–experimental approach, J. Therm. Anal. Calorim. 141 (5) (2020) 1703–1715.

[28] Y. Zhao, Q. Li, B. Zou, T. Zhang, L. Jin, G. Qiao, B. Nie, Y. Huang, Y. Ding, Performance of a liquid cooling-based battery thermal management system with a composite phase change material, Int. J. Energy Res. 44 (6) (2020) 4727–4742.

[29] J. Li, H. Zhang, Thermal characteristics of power battery module with composite phase change material and external liquid cooling, Int. J. Heat Mass Transf. 156 (2020) 119820.

[30] M. Rabiei, A. Gharehghani, A.M. Andwari, Enhancement of battery thermal management system using a novel structure of hybrid liquid cold plate, Appl. Therm. Eng. (2023) 121051.

[31] S. Ki, J. Lee, S. Kim, J. Seong, J. Shim, S. Oh, S. Cho, S. Bang, D. Seo, J. Kim, An energy-efficient battery thermal management system incorporating a porous metal-based multiscale flow manifold, Energ. Conver. Manage. 269 (2022) 116147.

[32] A. Moaveni, M. Siavashi, S. Mousavi, Passive and hybrid battery thermal management system by cooling flow control, employing nano-PCM, fins, and metal foam, Energy 288 (2024) 129809.

[33] V. Choudhari, A. Dhoble, S. Panchal, Numerical analysis of different fin structures in phase change material module for battery thermal management system and its optimization, Int. J. Heat Mass Transf. 163 (2020) 120434.

[34] M.M. Heyhat, S. Mousavi, M. Siavashi, Battery thermal management with thermal energy storage composites of PCM, metal foam, fin and nanoparticle, J. Storage Mater. 28 (2020) 101235.

[35] Y. Lv, X. Yang, X. Li, G. Zhang, Z. Wang, C. Yang, Experimental study on a novel battery thermal management technology based on low density polyethylene-enhanced composite phase change materials coupled with low fins, Appl. Energy 178 (2016) 376–382.

[36] E. Aslan, Y. Aydın, Y. Yaşa, Consideration of graphene material in PCM with aluminum fin structure for improving the battery cooling performance, Int. J. Energy Res. 46 (8) (2022) 10758–10769.

[37] P. Zare, N. Perera, J. Lahr, R. Hasan, A novel thermal management system for cylindrical lithium-ion batteries using internal-external fin-enhanced phase change material, Appl. Therm. Eng. 238 (2024) 121985.

[38] P. Zare, N. Perera, J. Lahr, R. Hasan, Uniform temperature distribution, prolonged temperature regulation, and accelerated recovery of battery thermal management system using a novel fin design, J. Storage Mater. 108 (2025) 115054.

[39] W. Jiang, G. Feng, H. Wang, Z. Chang, X. Tan, J. Ji, Y. Zhang, J. Zhou, Analysis of hybrid active-passive prismatic Li-ion battery thermal management system using phase change materials with porous-filled mini-channels, J. Storage Mater. 80 (2024) 110144.

[40] S. Sarvar-Ardeh, R. Rafee, S. Rashidi, Enhancing the performance of liquid-based battery thermal management system by porous substrate minichannel, J. Storage Mater. 71 (2023) 108142.

[41] P. Jindal, R. Katiyar, J. Bhattacharya, Evaluation of accuracy for Bernardi equation in estimating heat generation rate for continuous and pulse-discharge protocols in LFP and NMC based Li-ion batteries, Appl. Therm. Eng. 201 (2022) 117794.

[42] Y. Miao, P. Hynan, A. Von Jouanne, A. Yokochi, Current Li-ion battery technologies in electric vehicles and opportunities for advancements, Energies 12 (6) (2019) 1074.

[43] E. Jiaqiang, M. Yue, J. Chen, H. Zhu, Y. Deng, Y. Zhu, F. Zhang, M. Wen, B. Zhang, S. Kang, Effects of the different air cooling strategies on cooling performance of a lithium-ion battery module with baffle, Appl. Therm. Eng. 144 (2018) 231–241.

[44] F. Zhang, F. Lu, B. Liang, Y. Zhu, H. Gou, K. Xiao, Y. He, Thermal performance analysis of a new type of branch-fin enhanced battery thermal management PCM module, Renew. Energy 206 (2023) 1049–1063.

[45] P. Taheri, M. Yazdanpour, M. Bahrami, Transient three-dimensional thermal model for batteries with thin electrodes, J. Power Sources 243 (2013) 280–289.

[46] S. Ambekar, P. Rath, A. Bhattacharya, A novel PCM and TCE based thermal management of battery module, Therm. Sci. Eng. Prog. 29 (2022) 101196.

[47] Zhang, H., H.W. Mu, Y. Zhang, and J. Han, *Calculation and characteristics analysis of lithium ion batteries' internal resistance using HPPC test.* advanced materials research, 2014. **926**: p. 915-918.

[48] S. Xin, C. Wang, H. Xi, Thermal management scheme and optimization of cylindrical lithium-ion battery pack based on air cooling and liquid cooling, Appl. Therm. Eng. 224 (2023) 120100.

[49] Y. Lai, W. Wu, K. Chen, S. Wang, C. Xin, A compact and lightweight liquid-cooled thermal management solution for cylindrical lithium-ion power battery pack, Int. J. Heat Mass Transf. 144 (2019) 118581.

[50] C. Zhao, W. Cao, T. Dong, F. Jiang, Thermal behavior study of discharging/charging cylindrical lithium-ion battery module cooled by channeled liquid flow, Int. J. Heat Mass Transf. 120 (2018) 751–762.

[51] V.R. Voller, C. Prakash, A fixed grid numerical modelling methodology for convection-diffusion mushy region phase-change problems, Int. J. Heat Mass Transf. 30 (8) (1987) 1709–1719.

[52] M. Fadl, P.C. Eames, Numerical investigation of the influence of mushy zone parameter Amush on heat transfer characteristics in vertically and horizontally oriented thermal energy storage systems, Appl. Therm. Eng. 151 (2019) 90–99.

[53] M. Bamdezh, G. Molaeimanesh, S. Zanganeh, Role of foam anisotropy used in the phase-change composite material for the hybrid thermal management system of lithium-ion battery, J. Storage Mater. 32 (2020) 101778.

[54] J.M. Mahdi, E.C. Nsofor, Melting enhancement in triplex-tube latent heat energy storage system using nanoparticles-metal foam combination, Appl. Energy 191 (2017) 22–34.

[55] A.A. Al-Abidi, S. Mat, K. Sopian, M. Sulaiman, A.T. Mohammad, Internal and external fin heat transfer enhancement technique for latent heat thermal energy storage in triplex tube heat exchangers, Appl. Therm. Eng. 53 (1) (2013) 147–156.

[56] Y. Tian, C.-Y. Zhao, A numerical investigation of heat transfer in phase change materials (PCMs) embedded in porous metals, Energy 36 (9) (2011) 5539–5546.

[57] J.G. Fourie, J.P. Du Plessis, Pressure drop modelling in cellular metallic foams, Chem. Eng. Sci. 57 (14) (2002) 2781–2789.

[58] X. Yang, T.J. Lu, T. Kim, An analytical model for permeability of isotropic porous media, Phys. Lett. A 378 (30–31) (2014) 2308–2311.

[59] Z. Liu, Y. Yao, H. Wu, Numerical modeling for solid–liquid phase change phenomena in porous media: Shell-and-tube type latent heat thermal energy storage, Appl. Energy 112 (2013) 1222–1232.

[60] P. Wang, X. Wang, Y. Huang, C. Li, Z. Peng, Y. Ding, Thermal energy charging behaviour of a heat exchange device with a zigzag plate configuration containing multi-phase-change-materials (m-PCMs), Appl. Energy 142 (2015) 328–336.

[61] M. Maerefat, S.Y. Mahmoudi, K. Mazaheri, Numerical simulation of forced convection enhancement in a pipe by porous inserts, Heat Transfer Eng. 32 (1) (2011) 45–56.

[62] D. Hacen, A. Boughamoura, S.B. Nasrallah, Forced pulsating flow and heat transfer in a tube partially filled with a porous medium, J. Porous Media 9 (1) (2006).

[63] B. Alazmi, K. Vafai, Constant wall heat flux boundary conditions in porous media under local thermal non-equilibrium conditions, Int. J. Heat Mass Transf. 45 (15) (2002) 3071–3087.

[64] Calmidi, V.V. and R.L. Mahajan, *The effective thermal conductivity of high porosity fibrous metal foams.* 1999.

[65] V.V. Calmidi, R.L. Mahajan, Forced convection in high porosity metal foams, J. Heat Transfer 122 (3) (2000) 557–565.

[66] C.-C. Chen, P.-C. Huang, H.-Y. Hwang, Enhanced forced convective cooling of heat sources by metal-foam porous layers, Int. J. Heat Mass Transf. 58 (1–2) (2013) 356–373.

[67] A. Amiri, K. Vafai, Analysis of dispersion effects and non-thermal equilibrium, non-Darcian, variable porosity incompressible flow through porous media, Int. J. Heat Mass Transf. 37 (6) (1994) 939–954.

[68] A. Amiri, K. Vafai, T. Kuzay, Effects of boundary conditions on non-Darcian heat transfer through porous media and experimental comparisons, Numer. Heat Transf. A Appl. 27 (6) (1995) 651–664.

[69] H. Xu, Z. Qu, W. Tao, Analytical solution of forced convective heat transfer in tubes partially filled with metallic foam using the two-equation model, Int. J. Heat Mass Transf. 54 (17–18) (2011) 3846–3855.

[70] Y. Mahmoudi, N. Karimi, Numerical investigation of heat transfer enhancement in a pipe partially filled with a porous material under local thermal non-equilibrium condition, Int. J. Heat Mass Transf. 68 (2014) 161–173.

[71] Roache, P.J., *Perspective: a method for uniform reporting of grid refinement studies.* 1994.

[72] Division, A.S.o.M.E.F.E., *Quantification of Uncertainty in Computational Fluid Dynamics*. 1993: American Society of Mechanical Engineers.

[73] R. Oliveira, G. Justi, G. Lopes, Grid convergence study of a cyclone separator using different mesh structures, Chem. Ind. Chem. Eng. Q. 23 (3) (2017) 311–320.

[74] X. Hu, F. Zhu, X. Gong, Experimental and numerical study on the thermal behavior of phase change material infiltrated in low porosity metal foam, J. Storage Mater. 26 (2019) 101005.

[75] M. Amani, M. Ameri, A. Kasaeian, The experimental study of convection heat transfer characteristics and pressure drop of magnetite nanofluid in a porous metal foam tube, Transp. Porous Media 116 (2017) 959–974.

[76] L.-L. Tian, X. Liu, S. Chen, Z.-G. Shen, Effect of fin material on PCM melting in a rectangular enclosure, Appl. Therm. Eng. 167 (2020) 114764.
[77] M. Torabi, K. Zhang, G. Yang, J. Wang, P. Wu, Heat transfer and entropy generation analyses in a channel partially filled with porous media using local thermal non-equilibrium model, Energy 82 (2015) 922–938.
[78] J. Zhang, X. Li, G. Zhang, H. Wu, Z. Rao, J. Guo, D. Zhou, Experimental investigation of the flame retardant and form-stable composite phase change materials for a power battery thermal management system, J. Power Sources 480 (2020) 229116.
[79] Saha, S.K., H. Ranjan, M.S. Emani, and A.K. Bharti, *Performance evaluation criteria in heat transfer enhancement*. 2020: Springer.
[80] H. Shokouhmand, F. Jam, M. Salimpour, The effect of porous insert position on the enhanced heat transfer in partially filled channels, Int. Commun. Heat Mass Transfer 38 (8) (2011) 1162–1167.
[81] B. Parveez, N.A. Jamal, H. Anuar, Y. Ahmad, A. Aabid, M. Baig, Microstructure and mechanical properties of metal foams fabricated via melt foaming and powder metallurgy technique: A review, Materials 15 (15) (2022) 5302.